ICARUS **132,** 1–35 (1998)
ARTICLE NO. IS975863

Compositional Evolution of Saturn's Rings Due to Meteoroid Bombardment

Jeffrey N. Cuzzi

Space Sciences Division, Mail Stop 245-3, Ames Research Center, Moffett Field, California 94035-1000
E-mail: cuzzi@cosmic.arc.nasa.gov

and

Paul R. Estrada

Astronomy Department, Space Sciences Building, Cornell University, Ithaca, New York 14853

Received April 10, 1997; revised October 6, 1997

In this paper we address the question of compositional evolution in planetary ring systems subsequent to meteoroid bombardment. The huge surface area to mass ratio of planetary rings ensures that this is an important process, even with current uncertainties on the meteoroid flux. We develop a new model which includes both direct deposition of extrinsic meteoritic "pollutants" and ballistic transport of the increasingly polluted ring material as impact ejecta. Our study includes detailed radiative transfer modeling of ring particle spectral reflectivities based on refractive indices of realistic constituents.

Voyager data have shown that the lower optical depth regions in Saturn's rings (the C ring and Cassini division) have *darker and less red* particles than the optically thicker A and B rings. These coupled structural–compositional groupings have never been explained; we present and explore the hypothesis that global scale color and compositional differences in the main rings of Saturn arise naturally from extrinsic meteoroid bombardment of a ring system which was initially composed primarily, but not entirely, of water ice. We find that the regional color and albedo differences can be understood if all ring material was initially water ice colored by tiny amounts of intrinsic reddish, plausibly organic, absorber, which then evolved entirely by addition and redistribution of extrinsic, nearly neutrally colored, plausibly carbonaceous material. The regional compositional differences result from different susceptibilities to pollution of regions with very different surface mass density.

We further demonstrate that the detailed radial profile of color across the abrupt B ring–C ring boundary can constrain key unknown parameters in the model. We carefully reanalyze and revise meteoroid flux estimates by Cuzzi and Durisen (1990, *Icarus* 84, 467–501) and estimate the duration of the exposure to extrinsic meteoroid flux of this part of the rings, at least, to be on the order of 10^8 years. This conclusion is easily extended by inference to the Cassini division and its surroundings as well. This geologically young "exposure age" is compatible with time scales estimated elsewhere based on the evolution of ring structure due to ballistic transport and also with other "short time scales" estimated on the grounds of gravitational torques. However, uncertainty in the flux of interplanetary debris and in the ejecta yield may preclude ruling out a ring age as old as the Solar System at this time. © 1998 Academic Press

I. INTRODUCTION

1.1. *Overview on Ring Composition*

Since the Voyager encounters with Saturn, the composition of the rings has received little attention relative to their surprisingly complex structure. Water ice has long been accepted as the most prominent component of ring composition (see reviews by Cuzzi *et al.* (1984) and Esposito *et al.* (1984). However, there is a rather large overall decrease in reflectivity (blue absorption) shortward of 0.6 μm wavelength, giving the rings a slightly non-gray, very pale tan or salmon color (Estrada and Cuzzi 1996; henceforth EC96). These properties require some non-icy constituents of as-yet unidentified nature (Lebofsky *et al.* 1970, Lebofsky and Fegley 1976, Clark 1980, Clark and McCord 1980, Cuzzi *et al.* 1984, Esposito *et al.* 1984). Whereas these visible and near-IR spectra refer only to the top millimeter or less of the surface, microwave observations probably sample the bulk of the ring mass. Interpretations of the microwave data constrain the mass fraction of any non-icy material to be less than 10% (Cuzzi *et al.* 1980, Epstein *et al.* 1980, 1984) and perhaps even less than 1% (Grossman 1990) by mass if uniformly distributed.

Ring photometry by Voyager 1 revealed that the main ring regions differed significantly in the albedo of their constituent particles; Smith *et al.* (1982) showed that the C ring and Cassini division particles had single scattering

0019-1035/98 $25.00
Copyright © 1998 by Academic Press
All rights of reproduction in any form reserved.

albedo of 0.15–0.2, while the B and A ring particles had single scattering albedo of 0.4–0.5 (see also Cuzzi *et al.* 1984). These conclusions have been confirmed and refined by subsequent work (Dones *et al.* 1993, Doyle *et al.* 1989, Cooke 1991). Even the higher A and B ring particle albedos are much too low for impurity-free ice. Voyager data (Smith *et al.* 1982, EC96) also show that the ring colors vary significantly on both regional and local radial scales (Fig. 1). A general grouping thus appears such that the lower optical depth regions (the C ring and Cassini division) have *darker and less red* (not "more blue") particles than the optically thicker A and B rings (EC96). These coupled structural–compositional groupings have never been explained; in this paper we present and explore a hypothesis that global scale color and compositional differences in the main rings of Saturn arise naturally from extrinsic meteoroid bombardment of a ring system which was initially composed primarily, but not entirely, of water ice.

1.2. Meteoroid Bombardment as a Process

Because of their huge ratio of area to mass, ring systems are far more susceptible to the effects of extrinsic bombardment than the solid surfaces on which the effects of impacts have long been known to play a role. Estimates of the bombarding flux by Morfill *et al.* (1983), Ip (1984), and Cuzzi and Durisen (1990, henceforth CD90) differ somewhat but all imply that Saturn's rings are impacted by close to their own mass over the age of the Solar System (discussed more in section 4.2).

Several "short time scale" aspects of the meteoroid bombardment process have been identified. Ip (1984) and Lissauer (1984) noted that meteoroid infall decreases the angular momentum per unit mass of the system, leading to some inward radial evolution. CD90, using their flux value, showed that this effect leads to loss of the C ring material into Saturn in 10^7–10^8 years. Doyle *et al.* (1989) noted that the relatively high albedo of the A and B ring particles was inconsistent with their having retained more than a small fraction of this presumably primitive, carbonaceous, "Halley dust." They suggested that this implied a geologically recent origin for these rings. These constraints are made even stronger if the rings are less than 1% non-icy material, as suggested by Grossman (1990; this strict 1% limit was not mentioned in the only publication of this work, by Grossman *et al.* (1989). Other short time scales are more closely related to the material ejected than the material remaining. Northrop and Connerney (1987) suggested that the loss to Saturn's ionosphere of water molecules and grains generated by impact could explain the unusually low ionospheric electron density, and obtained another youthful age for the rings. In a series of papers, Durisen and colleagues (1984, 1989, 1992, 1996) have described the structural influence of meteoroid bombardment and found that certain otherwise unexplained aspects of ring *structure* do seem to be natural byproducts of what is referred to as "ballistic transport" of meteoroid ejecta. These include the fairly abrupt inner edges of the A and B rings, the very similar linear "ramps" connecting them to the Cassini division and C ring, respectively, and possibly also the "irregular structure" found in the inner A and B rings. The subject has been reviewed recently by Porco (1995) and Cuzzi (1995).

1.3. Goals of This Work

Our task was to see (a) whether the meteoroid bombardment process is qualitatively consistent with regional and local compositional (color) differences in Saturn's ring system and (b) to see whether yet another independent estimate of ring age might be obtained by comparing these models with the data of EC96. We will make use of certain aspects of the numerical models and conclusions of Durisen *et al.* (1989, 1992). The models we describe in this paper share several parameters with the structural evolution models, but they enter in slightly different ways. In the work of Durisen *et al.* (1989, 1992), local mass density is largely conserved by a high-order balance between the small amount of material which is transported directly by a great distance, and a small radial reflex adjustment by a much larger amount of local ring material. These models do not follow actual parcels of matter, but instead treat the ring material as homogeneous everywhere. Our models *do* keep track of the radial evolution of materials of different composition, incorporate accurate modeling of all the ejecta and orbital dynamics and include our best estimates of ring viscosity. On the other hand, the models presented here do not allow ring *structure* to evolve; this simplifying assumption is discussed further below. Also, the work presented here relates to an entirely independent data set and thus provides an independent constraint.

Using these models, we conclude that the extrinsic bombardment/ballistic transport process not only holds up well under this scrutiny, but in fact provides a straightforward explanation for the coupled structural and compositional properties of Saturn's main rings. Furthermore, radial compositional variation resembling that which is observed in Saturn's rings is apparently produced by the ballistic transport process in a small fraction of the age of the Solar System.

In Section 2 we provide an overview of our methodology, and in Sections 3 and 4, we give a detailed two-part description of our model. In Section 5 we focus on refractive indices of the ring material at two "typical" end-point locations. In Section 6 we discuss how detailed radial profiles provide a good constraint on the ring age. In Section 7 we discuss the implications and note several lines of future work that would be of interest. The numerous parameters are summarized in Table 4 at the end of the paper.

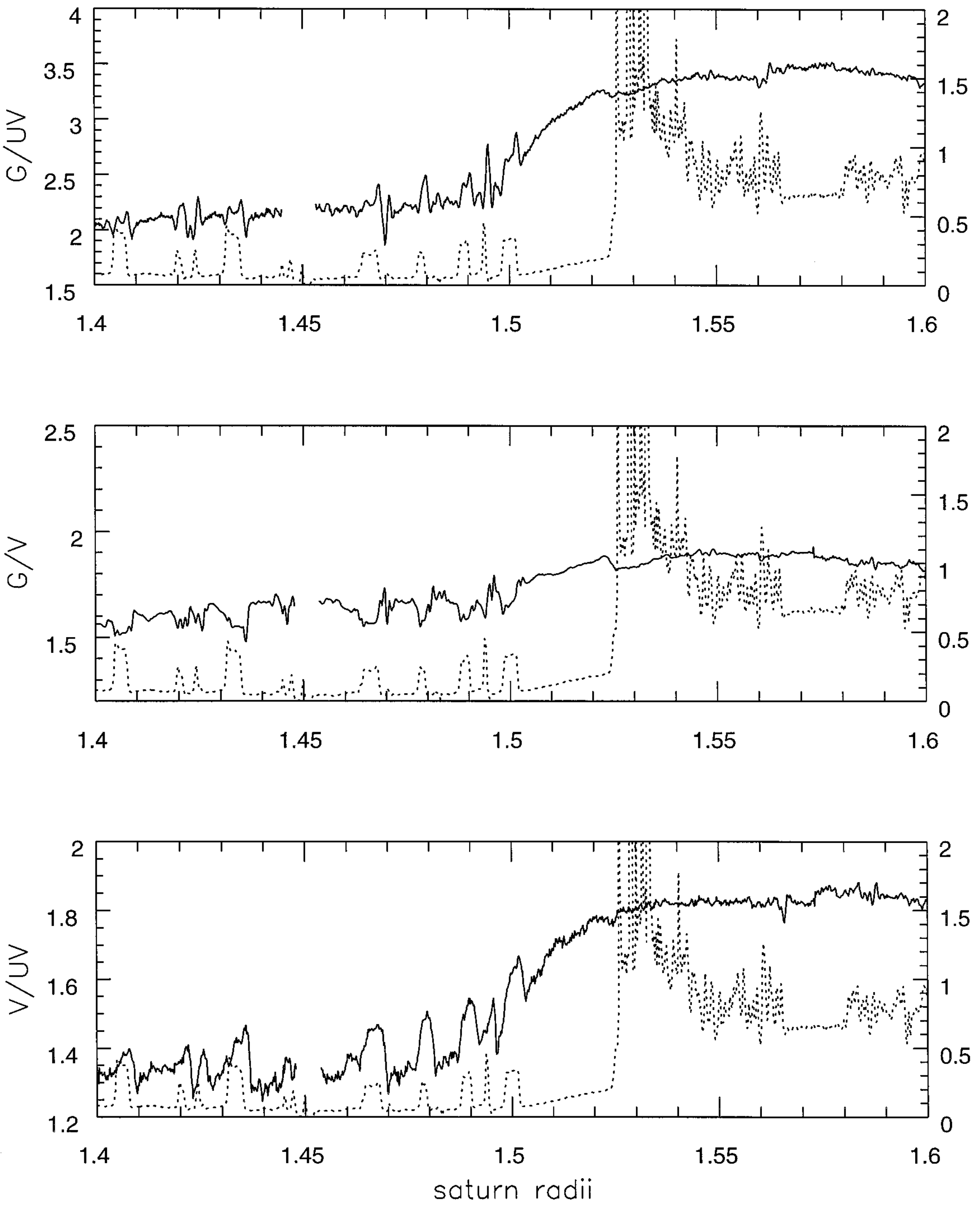

FIG. 1. Solid lines show the radial profiles of color ratio between brightness in Voyager *G*, *V*, and *UV* filters, in the radial region of interest here (from Estrada and Cuzzi 1996). The inner edge of the B ring is at $1.525r_S$. Dotted lines show the radial profile of normal optical depth in the Voyager Clear filter, for which the vertical scale is from 0.0 to 2.0.

2. OVERVIEW OF METHODOLOGY

We assume that the rings all originate with some uniform "primordial" composition (primarily water ice); we hypothesize that radial changes in composition result only from extrinsic meteoroid bombardment. In this initial paper, we model the inner edge of the B ring and its transition to the C ring. Our methodology is rather novel and, although conceptually simple, draws on many different elements. Before describing any of it in detail, we present here a very schematic sketch of the logic.

(1) We argue that the illumination and viewing geometry simplifies the radiative transfer to the extent that all

multiple scattering may be neglected and thus that observed profiles of *reflectivity* ratio (at two different wavelengths) translate into profiles of *albedo* ratio (Section 3.1). The particle albedo is modeled using a Hapke-type regolith radiative transfer approach. Individual regolith grains are taken as independent scatterers with wavelength-dependent refractive indices (Sections 3.2, 3.3). A phase space of ring particle albedo ratio between Voyager *UV* (345 nm), *V* (413 nm), and *G* (562 nm) filter passbands and average (Clear filter) albedo is constructed (Section 3.4). We explore the evolution of ring particle color and albedo in this phase space as one sort of material is admixed with another, and illustrate the utility of this approach with some comments about satellites in the Jupiter and Saturn systems.

(2) In Section 4 we describe our model of the ''pollution transport'' which results from deposition of meteoritic material and its distribution by subsequent impact ejecta. We first parametrize the ring normal optical depths $\tau(r)$ and mass densities $\sigma(r)$ (Section 4.1). We then discuss the meteoritic flux and its direct effects (Section 4.2). We next describe how two independent points in the rings would evolve differently, depending on their local optical depth and mass density (Section 4.3). In Section 4.4. we describe our numerical model for ballistic transport of ejecta and redistribution of ''pollutants,'' in which we track the detailed radial distributions of both the temporally increasing extrinsic component with mass fraction $f_e(r, t)$, and a primordial (icy) component with abundance $1 - f_e(r, t)$. We use those parts of the numerical code of Durisen *et al.* (1989, 1992) which calculate the mass transferred between any radius and any other radius; radial drifts are accounted for in an approximate fashion. As material is transferred from place to place, the new constituents are assumed to be uniformly mixed with material previously there while the total $\sigma(r)$ and $\tau(r)$ are assumed to remain the same. The transport model is parameterized by ejecta yield and velocity distribution, as discussed by CD90 and Durisen *et al.* (1992), and by one new parameter setting the *retention efficiency* (η) with which extrinsic (absorbing) material retains its optical properties after hypervelocity impact (Doyle *et al.* 1989).

(3) In Section 5, we use this methodology to determine ring particle refractive indices. Initially, two extreme radial points (1.40 and 1.60 Saturn radii) are used with our albedo–color phase relationship to determine the current ring particle refractive indices at these locations. As in Section 4.3, the two regions are treated as of identical initial composition, evolving independently due merely to local deposition of meteoritic material. We seek a combination of candidate refractive indices at three wavelengths and the mass mixing ratios implied by those values. The ''primordial'' ring composition is inferred by correcting for its accumulated component of extrinsic material, using scaling arguments. It appears most likely that the rings initially contained a small admixture of fairly red material and have been polluted over time by fairly neutral, extrinsic material (Section 5.1).

(4) Average material refractive indices are converted to mass fractions of water ice f_i, initial intrinsic non-icy absorber f_a, and extrinsic meteoritic material f_e by comparison with plausible candidate intrinsic and extrinsic materials of the proper spectral shape. Several known candidate materials have properties consistent with these non-icy constituents; their fractions must remain consistent with constraints on the total non-icy material set by other observations (Section 5.2). Mass mixing ratios result for different materials which reflect only the *cumulative fluence* of material, and can provide an age constraint only if both the mass *flux* reaching the rings, $\dot{\sigma}_e$, and the efficiency, η, are known.

(5) In order to resolve this ambiguity we resort to detailed modeling of the shapes of radial profiles. In Section 5.3, detailed modeling of radial profiles using our transport model is presented, using the methodology of Section 4. A radial profile of ring particle albedo ratio, between appropriate Voyager filters, is calculated as in (2) above. The *shape* of the C ring–B ring transition depends on a combination of model parameters which allows us to establish the ring exposure time in units of the ''gross erosion time'' $t_g \approx \sigma/(Y_0\dot{\sigma}_e)$, where Y_0 is ejecta yield. These profiles are compared with observed color ratio profiles (Estrada and Cuzzi 1996).

(6) The end result is an optimum combination of model parameters that gives an estimate for the primordial ring composition and, in principle, an actual age for the rings in terms of the extrinsic mass flux $\dot{\sigma}_e$ and ejecta yield Y_0 (Section 5.4). Current estimates of flux and ejecta yield lead to exposure ages much less than the age of the Solar System, but this conclusion remains subject to uncertainties in the impact ejecta yield and the extrinsic mass flux.

3. RADIATIVE TRANSFER

In the next few subsections, we describe our approach to modeling the spectral reflectivity of the rings for comparison with observations. This primarily involves modeling the albedo of the ring particles from material refractive indices; our ratio approach suppresses any dependence on particle phase function or ring layer effects.

3.1. Ring Layer Reflectivity

Voyager imaging observations provide the reflectivity of the rings over a range of specific illumination and viewing geometries; the reader is referred to Cuzzi *et al.* (1984) for basic aspects of ring photometry and additional references. In the backscattering, low ring tilt angle Voyager geometry, the ring reflectivity I/F is very well approximated by neglecting multiple scattering (Cuzzi *et al.* 1984, Cooke 1991, Dones *et al.* 1993, EC96),

$$\frac{I}{F} = \frac{S}{4\mu} = \frac{1}{4\mu} A_\lambda P_\lambda \frac{\mu\mu_0}{\mu + \mu_0}\left[1 - \exp\left(-\tau\frac{\mu + \mu_0}{\mu\mu_0}\right)\right], \quad (1)$$

where the incident flux is πF, S is the scattering function, μ is the cosine of the emission angle, μ_0 is the cosine of the incidence angle, and A_λ and P_λ are the particle albedo and phase function, respectively (Chandrasekhar 1960; cf also Cuzzi *et al.* 1984).

Uncertainties in the scattering function S of a realistic ring layer due to effects such as particle packing volume translate into uncertainties in the derived ring particle albedo (Dones *et al.* 1989, Cooke 1991, Dones *et al.* 1993). However, these uncertainties relate primarily to the exact dependence of S on τ and geometrical parameters. The observations (Dones *et al.* 1993, EC96) support a single scattering hypothesis. If multiple scattering were important, color differences would be accentuated in optically thicker regions and observed radial variations in color ratios would show a strong correlation with optical depth variations. In fact, the case is quite the opposite with the exception of some narrow regions which are well removed from the B–C boundary under discussion here (EC96). Therefore, whatever the form of S, the mere dominance of single scattering ensures a linear dependence of I/F on A_λ.

In this paper, we will work primarily with ratios of the observed I/F at different wavelengths and will treat them as ratios of ring particle albedo at those wavelengths. Our primary modeling effort is in obtaining estimates of ring particle *albedo* from wavelength-dependent refractive indices (Section 3.2). This is equivalent to assuming that all other factors describing the scattering properties of the layer as a whole, including the ring particle phase function P_λ and the optical depth τ, are wavelength independent. A wavelength-independent optical depth seems quite reasonable; the optical depth of Saturn's main rings at visual wavelengths is dominated by particles that are much larger than a wavelength and well into the range of geometric optics. The assumption of wavelength-independent phase function is less clear cut (see Section 3.3) but probably reasonable away from strong absorption bands.

3.2. Ring Particle Albedo

Modeling the albedo of a granular regolith is usually done by analogy with a classical, semi-infinite scattering medium which is composed of many independent scatterers. Each scatterer, or grain, has its own single-scattering albedo and phase function. The ring particle regolith is considered to be an opaque cloudy atmosphere which is locally plane-parallel. This is accomplished by adjusting a variety of parameters within different sets of functional forms purported to represent the physical situation Hapke 1981, Lumme and Bowell 1981). Some degree of controversy attaches to different aspects of this modeling; questions as to the role of shadowing (both interparticle and surficial), diffraction, and packing effects in realistic regoliths render the various parameters of the models of uncertain diagnostic value and make calculation of reliable particle phase functions from basic principles problematic. However, in spite of the various pitfalls, it has been shown that such "first principles" calculations of *wavelength-dependent total reflectivity* from refractive indices can give good agreement with laboratory observations (Clark and Roush 1984).

To calculate the ring particle albedo A_λ, we will adopt the standard perspective that the ring particle regolith is composed of independent scatterers, or regolith grains, each having its own single scattering albedo ϖ_λ and its own elementary phase function which is characterized by asymmetry parameter g. We will assume "intimate mixing" of constituents; that is, all grains are assumed to be identical, with radius r_g, and each to be itself internally well mixed on a scale smaller than a wavelength. The effective grain refractive indices (n_r, n_i) are calculated using the mixing theory of J. C. Maxwell Garnett (see, e.g., Bohren and Huffman 1983). We have verified that, for the refractive indices of the individual constituents used here, where n_r (all materials) $\equiv n_{ra}, n_{ri}, n_{re}$ is on the order of unity, and $n_i(\text{ice}) \approx 0$ (Warren 1984), a simple volume-weighted mixing model is quite adequate even though n_i(initial absorber) $\equiv n_{ia} \sim 1$, because the mass fraction absorber f_a is so small. That is, $n_i \approx f_a n_{ia} \ll 1$ and $n_r = 1 + f_a(n_{ra} - 1) \approx 1$. For conceptual purposes, we will refer interchangeably to mass or volume weighted mixing models; volume weighting differs only by a weighting factor of the density of the solid.

Given the grain radius r_g and a set of refractive indices, we use the approach of Hapke (1981) to obtain the albedo of an individual regolith grain. This approach has several aspects. It assumes the regolith grain to be much larger than the wavelenth; this allows calculation of the grain albedo using ray optics, while accounting for multiple internal reflections using Fresnel coefficients. For our purposes, we use only the following expressions for the albedo of such an homogeneous grain with no additional internal scattering centers,

$$\varpi_\lambda = \frac{1}{1 + \alpha D_e} \quad (2)$$

(Hapke Eq. (33)), where $\alpha = 4\pi n_i/\lambda$,

$$D_e = \frac{4r_g}{3}\frac{1 - S_E}{1 - S_I} \quad (3)$$

(Hapke Eq. (32)), where S_E and S_I account for external and internal reflections and depend on material refractive indices (Hapke Eq. (22)):

$$S_E = \frac{(n_r - 1)^2 + n_i^2}{(n_r + 1)^2 + n_i^2} + 0.05 \tag{4}$$

$$S_I = 0.6125\sqrt{n_r}\log[(n_r + 1)^2 + n_i^2 - 3]. \tag{5}$$

The expression for S_I is our own fit to Hapke's Fig. 6 and is valid for $n_i^2 \ll 1$.

We adopt a "typical" regolith grain radius of $r_g = 20$ μm based on fits of the ratio of intensity in local reflectance maxima at 3.1 and 3.6 μm wavelengths in the water ice bands by Doyle *et al.* (1989). A similar result was obtained by Pollack *et al.* (1973) from bands at 1.5 and 2.0 μm. This effective distance between scattering centers characterizes whatever real particle size distribution exists in the ring particle regolith.

The grain albedo calculation discussed above makes no allowance for diffraction, but merely calculates the ratio of flux emergent from a grain to that incident upon its physical cross section. Because of the (relatively) close packing of regolith grains, diffraction is probably irrelevant and this treatment is not only appropriate but probably even desirable (Mischenko 1994). The scattering phase function of one of these regolith grains is modeled in an *ad hoc* fashion by a Henyey–Greenstein type function with asymmetry parameter g, where $g = -1$ for complete backscattering, $g = 1$ for complete forward scattering, and $g = 0$ for isotropic scattering. Even neglecting *diffracted* radiation, individual, nonspherical grains which are relatively smooth and have low absorption will favor forward scattering just from externally reflected and internally refracted light (Pollack and Cuzzi 1980, Mischchenko 1994).

Multiple scattering between grains is a critical aspect of regolith radiative transfer. Hapke (1981) assumes that multiple scattering within the regolith is completely isotropic and includes the grain phase function only as a first-order correction. Using this formulation, it is invariably found that icy, outer Solar System objects are best fit with $g \leq 0$. Lumme and Bowell (1981) improve on this somewhat by making use of similarity relations to relate the actual grain albedo to that of an equivalent isotropic scatterer (Irvine 1975); here, less negative or slightly positive values of g are found. Even using the Hapke version, terrestrial snowbanks, for which a considerable amount of data has been obtained, are characterized by $g = 0.6$ (Verbiscer *et al.* 1990). It is not understood why outer planet satellites differ in this way from terrestrial icy surfaces; Verbiscer *et al.* (1990) suggest tiny pits due to magnetospheric charged particles. Saturn's rings, as opposed to satellite surfaces, are largely free of this effect because the magnetospheric density is zero in the ring region. In fact, Cooke (1991) favors $g \sim 0.3$ for grains in the C ring particles, indicating that they may be different from those on icy satellite surfaces.

Mischchenko (1994) concludes, and we concur, that the *inference* of grain asymmetry parameter g *from* observed brightness variations is very difficult, due to the difficulty of inverting the multiple scattering problem. However, the value of g *does* influence the scattering history of a photon within the regolith and thus the spectral dependence of the emergent photons. Therefore, after using Eqs. (2)–(5) above (from the Hapke model) to calculate grain albedo, our approach diverges from the traditional Hapke modeling. We have made use of a formalism due to Van de Hulst (1980) that captures the effects of arbitrary anisotropic multiple scattering by regolith grains. This approach integrates the diffuse scattering function immediately over both incident and emission angles to produce the single scattering albedo that we need. Specifically, our ring particle albedo is the function

$$A_\lambda = 4\int\int R(\mu, \mu_0)\mu\mu_0 d\mu d\mu_0, \tag{6}$$

where

$$R(\mu, \mu_0) = \frac{I(\mu, \mu_0)}{\mu_0 F} \tag{7}$$

is the bidirectional reflectance of some (planar) facet of the surface of the ring particle. For comparison, $R(\mu, \mu_0) = 1$ represents a perfect Lambert reflector (Van de Hulst 1980, Cuzzi 1985). These numerically integrated functions are referred to as *URU* (Van de Hulst 1980; Vol. 1, pp. 37, 55, 68) and are presented in tabular form (Van de Hulst, Vol. 2, Fig. 11.3, Table 27 as "flux"). Van de Hulst has fit these functions using a similarity parameter

$$s_\lambda = \sqrt{\frac{1 - \varpi_\lambda}{1 - \varpi_\lambda g}}, \tag{8}$$

yielding

$$A_\lambda = \frac{(1 - s_\lambda)(1 - 0.139 s_\lambda)}{1 + 1.17 s_\lambda}. \tag{9}$$

This function is fully general for arbitrary grain albedo ϖ_λ and anisotropy parameter g, and we use it to calculate the ring particle spherical, or Bond, albedo A_λ given the (Hapke) grain albedo ϖ_λ (Eq. (2)) which we calculate for the effective (Maxwell Garnett) refractive indices (n_r, n_i). We treat the grain asymmetry parameter g as a parameter. A similar approach was also used by Doyle *et al.* (1989), who actually used Mie theory to calculate the grain albedo, thus incorporating diffraction and assuming well-separated grains, and then used the Van de Hulst scaling relationships as above.

The mass fraction inferred for any absorbing and/or extrinsic material, from visual wavelength color and albedo, is dependent upon whether or not the impurities are uniformly or nonuniformly mixed within the (presumedly) icy matrix. Doyle *et al.* (1989) found that the fractional mass inferred from a particle mixing model is essentially the same as that inferred from an intimate mixing model as long as the dark particles are smaller than 1 μm so in radius (a regime inappropriate for Hapke theory). Doyle *et al.* (1989) found that nonuniform mixing of any kind, and on any scale, greatly increases the mass of absorber needed to produce a given color and darkness. Specifically, they found that pure "absorber" particles larger than 10 μm quickly violate overall pollution fractions of 1–10% based on microwave observations. In addition, constant and vigorous hypervelocity meteoroid bombardment and ballistic transport makes it plausible that all ring material has been thoroughly mixed to very small (micrometer or submicrometer) grain size scales. Therefore, since particle mixing models require additional uncertain free parameters and, at best, convey no advantage to understanding the observations, all of our conclusions assume that the materials are intimately mixed, i.e., on size scales comparable to or smaller than a typical regolith grain.

3.3. *Ring Particle Phase Function*

Little is actually known about phase functions of icy regolith-covered objects such as the outer planet moons and ring particles. Dones *et al.* (1993) found that (clear filter) particle phase functions vary radially along with particle albedo throughout the A ring and suggested that this might be due to a surface compaction effect. Doyle *et al.* (1989) observed what appear to be significant variations in the clear filter phase functions of large B ring particles in and out of "spokes," suggesting that tiny spoke grains and regolith grains may exchange roles. In our case, however, the issue is whether large ring particle phase functions at a given angle in backscatter vary significantly as functions of *wavelength*, *away* from spokes.

Although there is evidence for wavelength-dependent phase functions of regolith-covered icy bodies at very small phase angles (Noland *et al.* 1974), this does not hold true at larger phase angles (Buratti and Veverka 1984). Buratti (1988) and Buratti *et al.* (1990a) discuss the general lack of significant variation of phase function with wavelength in the visual range for the satellites of Saturn. Similar conclusions are drawn for Triton and Miranda by Hillier *et al.* (1989, 1991). On the other hand, Buratti *et al.* (1990b) find that the phase function of Titania is more backscattering in the Voyager *UV* filter than in the green filter.

Our need is rather simple, because we deal with *ratios* of I/F at different wavelengths in and near the visual range, and at only one combination of phase, incidence, and emission angles. We argue that because the ring particles are overwhelmingly macroscopic, and the filters involved are broad and away from strong absorption features, variations in ring optical depth and ring particle phase function will be of lesser importance than in ring particle albedo.

3.4. *Phase Space of Ring Particle Albedo and Color*

For any pair of Voyager passbands, we define the *albedo ratio* $\mathscr{R}$ as the ratio of the I/F in the two filters at essentially the same geometry, as discussed above. That is, from Eq. (1),

$$\mathscr{R}_{\lambda_1,\lambda_2} = \frac{(I/F)_{\lambda_1}}{(I/F)_{\lambda_2}} \simeq \frac{A_{\lambda_1}}{A_{\lambda_2}}. \tag{10}$$

We will make use of a phase space in which a material is represented by both the ratio $\mathscr{R}$ and some average albedo $\overline{A}$. The average albedo could be any weighted combination of the two spectral albedos; we have chosen to use the albedo A_C as defined over the *clear filter passband*, instead of what might seem the more simple average of the albedos in the two filters in question. This was because the clear filter albedo is simpler to obtain from the observations. We define A_C as a linear combination of the albedos we calculate at our wavelengths of interest; $A_C = c_{UV}A_{UV} + c_G A_G$ (Appendix A). The coefficients we use for obtaining the appropriate clear filter albedo from our model albedos at the effective wavelengths of the G and UV filters, for each main ring region, are given in Table I. These coefficients depend on the shape of the spectrum; thus they differ slightly between different ring regions. However, they are independent of A_C; thus, either future improvements in knowledge of $A_{G,V,UV}$ or direct determination of A_C can then be used to easily update our results.

As the effective refractive index of the material varies with wavelength, the regolith grain albedo changes and thus the overall ring particle albedo changes, leading to different albedo ratios $\mathscr{R}_{\lambda_1\lambda_2}$. We have found that a helpful way of representing them is to define, over the wavelength range in question, a linearized function for the imaginary refractive index n_i:

$$n_\mathrm{i}(\lambda) = n_{\mathrm{i}UV} - a(\lambda - \lambda_{UV}). \tag{11}$$

Thus, the *intrinsic redness* of a material is parametrized by the coefficient a and its *intrinsic absorptivity* by the intercept $n_{\mathrm{i}UV}$. Within the phase space spanned by A and $\mathscr{R}$, characteristic contours of slope a and intercept $n_{\mathrm{i}UV}$ appear as shown schematically in Fig. 2. In a linear mixing approximation, where some mass fraction f_e of extrinsic material

TABLE I

Results Assuming Atmospheric Calibration
c_λ Coefficients

	B ring	C ring
c_{UV}	0.137	0.205
c_G	0.863	0.796

Albedo and imaginary index of refraction

	B ring		C ring	
$\lambda(\mu\text{m})$	A	$n_i \times 10^4$	A	$n_i \times 10^4$
0.3449 (UV)	0.14	4.36	0.09	7.34
0.4125 (V)	0.25	2.13	0.12	6.35
0.5622 (G)	0.47	0.778	0.18	4.78

Results Assuming Satellite Calibration
c_λ Coefficients

	B ring	C ring
c_{UV}	0.133	0.203
c_G	0.867	0.797

Albedo and imaginary index of refraction

	B ring		C ring	
$\lambda(\mu\text{m})$	A	$n_i \times 10^4$	A	$n_i \times 10^4$
0.3449 (UV)	0.16	3.56	0.10	6.15
0.4125 (V)	0.25	2.18	0.12	6.46
0.5622 (G)	0.46	0.807	0.18	4.87

with imaginary index n_{ie} has been added to material of initial imaginary index n_{io}, the mixture index n_i becomes (using Eq. (11))

$$\begin{aligned} n_i &= (1 - f_e)n_{io} + f_e n_{ie} \\ &= (1 - f_e)[n_{ioUV} - a_o(\lambda - \lambda_{UV})] \\ &\quad + f_e[n_{ieUV} - a_e(\lambda - \lambda_{UV})] \end{aligned} \tag{12}$$

and similarly for the quantity $(1 - n_r)$. For the present, because the real part of the refractive index n_r does not vary dramatically for icy, rocky, and organic materials over the visual wavelength range, and because these non-icy constituents are very small mass and volume fractions of the total, we take the overall real refractive index to be that of ice. Note that the spectral slope of the effective imaginary index of the mixture is

$$\frac{\partial n_i}{\partial \lambda} = (1 - f_e)\frac{\partial n_{io}}{\partial \lambda} + f_e \frac{\partial n_{ie}}{\partial \lambda} = (1 - f_e)a_o + f_e a_e. \tag{13}$$

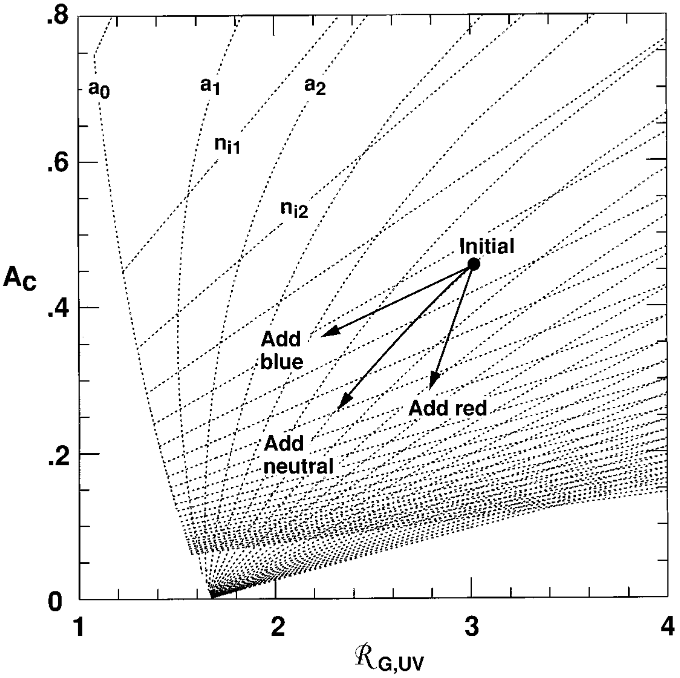

FIG. 2. Schematic of albedo–color phase space. A_C is the Bond or single scattering albedo of an object in the Voyager Clear filter, and $\mathcal{R}$ is the ratio of its reflectivity at two wavelengths (here, Green and UV). Each point in this phase space is characterized by some refractive index $n_i = n_{i,UV} - a(\lambda - \lambda_{UV})$. The values of a and $n_{i,UV}$ vary with the grain radius, r_g, and grain scattering asymmetry factor, g. The dotted lines represent contours of constant values of a and $n_{i,UV}$. As the grain refractive index changes, material "evolves" in this phase space; both the observed albedo *and* color of the object change. Three evolutionary paths are shown: adding neutral absorbing material ($a = 0$) does not change the *slope* of the composite; thus, evolution is along a curve of constant a if neutral material is the "pollutant" (curves denoted "add neutral." Adding material that is intrinsically "red" ($a > 0$) or "blue" ($a < 0$) produce the other trajectories, appropriately labeled, which *cross-over* contours of constant a.

Thererefore, adding neutral material ($a_e = 0$ or $n_{ie} =$ constant) *does not change the intrinsic redness of the mixture* as long as $f_e \ll 1$.

As its composition and effective refractive index change, material follows a certain characteristic path in albedo–color, or (A_C, $\mathcal{R}$) space. The specific "trajectory" of the surface depends on both the refractive indices of the initial material and those of the added pollutant. The cartoon in Fig. 2 illustrates these trajectories. Each of the curves labeled a_j represents material of a different "intrinsic redness," given by the spectral slope a_j of the refractive index. The curves labeled n_{ij} represent contours of the imaginary index at the Voyager UV wavelength. Addition of neutrally colored (constant imaginary index) material moves a surface along one of the contours of constant *intrinsic* redness (slope of imaginary index) so that the surface as a whole becomes generally *less red* as it darkens; addition of intrinsically reddish or bluish material moves the surface *across* the contours as indicated. The fact that objects with *no* intrinsic redness get slightly redder as they darken (leftmost contour $a_o = 0$ in Fig. 2) is because the absorption per unit length is proportional to the imaginary index divided by the wavelength (see α in Eq. (2)). For neutral material, this results in a slight decrease in grain albedo and thus large particle albedo as wavelength decreases. For intrinsically redder material, this small effect is overwhelmed by the intrinsic decrease of absorptivity with increasing wavelength.

3.4.1. Voyager calibration. As most users of Voyager photometry know, the standard published camera calibration factors (Danielson *et al.* 1981) are no longer valid and have been replaced by a canonical set developed within the Voyager project and usually referred to as the Johnson–Buratti factors (see EC96 for a discussion). There is a remaining unresolved discrepancy in the calibration of the Voyager *UV* filter that has the potential to affect our results. All recent calibrations indicate the cameras are less sensitive than as calibrated by Danielson *et al.* (1981); our adopted calibration (the so-called *atmospheric calibration*) is the least changed. A disjoint calibration set based on satellites indicates the most degradation (see, e.g., Buratti 1984); the widely used Johnson–Buratti calibration is merely the average of the two. (The $(I/F)_{UV}$ values we infer are thus about 10% smaller, and our $\mathscr{R}_{G,UV}$ and $\mathscr{R}_{V,UV}$ values 10% larger, than if we were to adopt the satellite calibration; thus our ring points would move to the left by this amount in $(A, \mathscr{R}_{V,UV})$ or $(A, \mathscr{R}_{G,UV})$ space if the satellite calibration were used. In Section 5.2.1 we show that this uncertainty has no significant implications for our inferences about ring composition.

3.4.2. Observed satellite properties. To test the usefulness of our color–albedo phase space representation, we determined the coordinates of the satellites of Saturn and Jupiter on such a phase space plot (Fig. 3), with their initials enclosed by circles and triangles, respectively. Their uncertainty is (very) approximately the size of the symbols. Our B and C ring results are also shown in Fig. 3. The values shown for the icy satellites are obtained from a variety of sources, tabulated in Table II.

For the moons of Jupiter, actual geometric albedos at the Voyager wavelengths were weighted to obtain effective Clear filter geometric albedos, and a Bond albedo was obtained using a known phase integral or, for Io, Europa, and Amalthea, adopting a nominal value of 0.75. We used recent determinations of phase integrals for Ganymede (0.78 ± 0.06) and Callisto (0.51 ± 0.06) from Buratti (pers. commun. 1995). The ratio $\mathscr{R}_{G,UV}$ is simply formed from the ratio of geometric albedos.

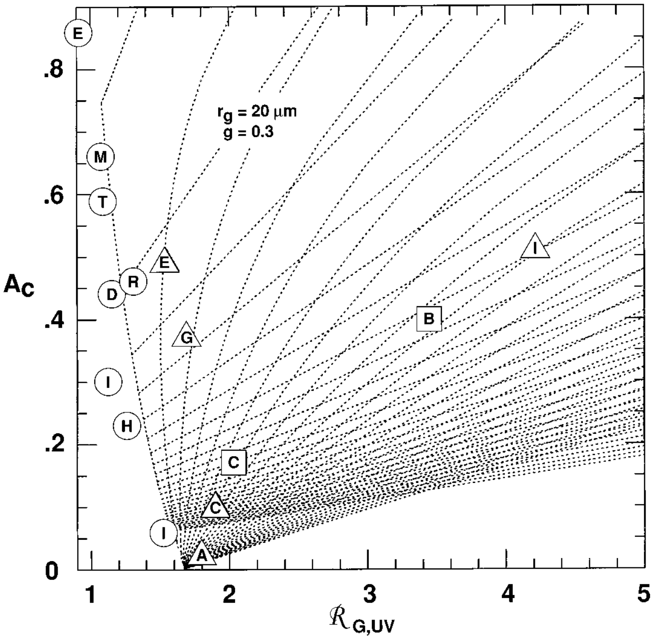

FIG. 3. Albedo–color ratio (G/UV) plot showing the attributes of the moons of Saturn (solid circles) and of Jupiter (triangles), as well as of our two primary points at $1.40 r_S$ in the C ring and $1.60 r_S$ in the B ring (squares). Within the context of the compositional evolution model we present here, both the rings and the icy moons of Saturn are consistent with addition of differing amounts of fairly neutral, or even slightly bluish, pollutant, while the moons of Jupiter seem better matched by a red pollutant (presumably from Io). Note, however, that the initial, prepollution composition of the rings is considerably redder than of the icy saturnian satellites. See Table II for specifics.

For the moons of Saturn, "visual" geometric albedos p_v were converted to Bond albedos using phase integrals for each moon. There is a difference between the "visual photometric" wavelength and that of the Voyager Clear filter that should be accounted for in future analyses along these lines. Various authors have presented normalized colorimetry for these moons; we thus obtained G/UV ratios for Mimas and Enceladus from Buratti (1984), and for Tethys, Dione, Rhea, Iapetus (dark and bright faces), and Hyperion from data summarized by Clark *et al.* (1984). Except for Iapetus, these are all globally averaged data. Pholus (2.2, 0.015; Cruikshank *et al.* 1996; Wilson *et al.* 1994) appears less red than either the B ring or Io on this plot, but would fall on a much redder "a" contour.

The icy moons of Saturn lie very close to the particular contour of constant intrinsic redness a which is the one for initially neutral material ($a \simeq 0$). That is, because their initial material is so nearly colorless, one can reconcile the combined variation of color and albedo for these moons with a single initial composition (neutral in color), with different admixtures of a *neutral* polluter. Buratti (1984) has previously noted that the darker saturnian satellites

TABLE II

Jupiter Satellites

Satellite	p_{UV}	p_G	$\mathscr{R}_{G,UV}$	q[a]	A_C[b]	Notes
Amalthea	N/A	N/A	1.79	0.75	0.02	[c]
Io	0.17	0.75	4.49	0.75	0.51	[d]
Europa	0.44	0.68	1.56	0.75	0.49	[e]
Ganymede	0.30	0.50	1.69	0.78	0.37	[f]
Callisto	0.11	0.21	1.90	0.51	0.10	[f]

Saturn Satellites[g]

Satellite	p_v[h]	$\mathscr{R}_{G,UV}$	q[i]	A_C[j]	Notes
Mimas	0.80	1.08	0.82	0.66	[k]
Enceladus	1.00	0.92	0.86	0.86	[k]
Tethys	0.80	1.09	0.74	0.59	[l]
Dione	0.55	1.15	0.80	0.44	[l]
Rhea	0.65	1.31	0.70	0.46	[l]
Hyperion	0.30	1.26	0.75	0.23	[l]
Iapetus (D)	0.08	1.52	0.75	0.06	[l]
Iapetus (B)	0.40	1.13	0.75	0.30	[l]

[a] Phase integrals q from Buratti (pers. commun. 1995) or assumed = 0.75.

[b] A_C from Eq. (A3).

[c] Gradie *et al.* (1980).

[d] Average of Johnson and Pilcher (1979), leading/trailing McFadden *et al.* (1980); cf. Clark (1980).

[e] Avg. of leading/trailing from McFadden *et al.* (1980); cf. Clark (1980).

[f] Avg. of leading/trailing from McFadden *et al.* (1980); cf. Clark (1980).

[g] Leading sides 10–40% brighter (Buratti 1984).

[h] Visual geometric albedos p_v from Cruikshank *et al.* (1984).

[i] Phase integrals q from Buratti (pers. commun. 1995) or assumed = 0.75.

[j] $A_C = qp_v$.

[k] Color ratios from Buratti (1984).

[l] Color ratios from Clark *et al.* (1984).

are redder. On the other hand, the icy moons of Jupiter are redder overall than the saturnian moons with comparable albedo, and they are a slightly poorer match to any curve of constant intrinsic redness. That is, the curve connecting them crosses contours of increasing redness as the albedo decreases, such as in curves denoted "add red" of Fig. 2. This implies that, if the jovian moons all began with the same initial composition, they have been polluted by *intrinsically red* material. This is not at all unreasonable; Io, which spews colored material into the magnetosphere and from there throughout the jovian system, is seen on the extreme red side of our phase space.

3.4.3. Observed ring reflectivity and particle albedo. Figure 3 also indicates by squares the properties of one location in the C ring and at one location in the B ring (r = 84,500 and 96,500 km, respectively, or $1.40r_S$ and $1.60r_S$). To reduce sensitivity to small local variations, we average our $\mathscr{R}$ values over local regions 3000 km wide at the nominal positions. *Both* points are considerably redder than the saturnian moons shown, especially the B ring—but compatible with adding a mostly neutral-to-slightly bluish pollutant to "B ring" material in order to obtain darker, and less red, C ring material. The general theme of our modeling is that the C ring differs from the B ring primarily in having accumulated and retained a larger mass fraction of (roughly) neutral material. While the locations of both the saturnian moons and rings in $(A_C, \mathscr{R})$ space are consistent with the appropriateness of neutral-to-slightly bluish extrinsic material as a pollutant for the Saturn system in general, the different behavior of the jovian moons implies that this consistency is not trivial.

Our approach to defining the values of A_C for these points is somewhat more complicated than for the moons. At the inner point, which is in the C ring, we use the results of Cooke (1991, Figs. 5.17–5.20), who modeled Voyager C ring photometry over a sufficient range of phase angles to separate albedo and phase function effects. In the C ring, the "classical" single-scattering S and T functions assumed by Cooke (1991) are probably good representations for the ring scattering function. Cooke obtained a small range of (Clear filter) ring particle single scattering albedos at this location, for several candidate phase functions. From her Fig. 5.17 we adopt a C ring particle albedo at this location of $A_C = 0.17 \pm 0.01$.

Obtaining a comparable value at the outer range of our modeled region, at 96,500 km in the B ring, is more difficult. It is known that scattering functions from a classical, many-particle-thick layer, are unable to explain the dramatic fluctuations in ring brightness seen throughout the A and B rings (Dones *et al.* 1989, 1993); thus the approach of Cooke (1991) may not apply. If the albedo is obtained by simultaneous solution of a wide range of phase and viewing angles, however, all unknown angular variation from the combination of particle phase function and layer effects can be removed together. We will make and use an estimate of the ring particle albedo at our benchmark radius by scaling from those obtained in this way from surrounding regions.

We solved for the ring particle albedo using one high and one low phase angle measurement of I/F from the scans in Fig. 3 of Cuzzi *et al.* (1984). The geometry-dependent part of the scattering function (Eq. (1)) is approximated by $\mu_0/(\mu + \mu_0)$ to very good accuracy for the optical depths and geometry involved, and we used this factor to derive the product $A_\lambda P_\lambda$ from observed reflectivities. We then solved for particle albedo and power law single-scattering phase functions $P(\Theta) = c_q\Theta^{-q}$ (i.e., for index q) at several locations in the B ring. For our inner B ring point, we used the I/F in the featureless band at 95,000 km, which has the lowest optical depth in the region and is more likely to be well modeled by the classical scattering function. In the B ring regions, where other, more accurate albedo values have been obtained (Doyle *et al.* 1989), our approximate values were close to but slightly lower than previously published values. We obtained a correction factor based on the ratio of our albedos to those of Doyle *et al.* in these overlap regions (112,000–116,000 km) and applied it to scale our derived albedo in the inner B ring. The phase function power law indices that resulted from this solution technique were around 2.4 in the B ring, quite compatible with values determined by Cooke (1991) in the outer C ring and C ring ramp. Doyle *et al.* (1989) preferred a Callisto-like phase function, with $q \sim 3.3$ (Dones 1987, Table 6.1), but their albedos do not change dramatically if they assume a Europa-like phase function, which is rather closer to $q \sim 2.9$ judging from Fig. 6.4 and Table 6.1 in Dones (1987). Our adopted ring particle albedo at 96,500 km is 0.40 ± 0.03; our uncertainty range is bounded at the high end by the range of albedos (0.54–0.58) in Doyle *et al.* (1989) and at the low end by both the results of Cooke (1991; 0.35 ± 0.1) and the alternate scaling constants obtained from the results of Dones *et al.* (1993) in the A ring. This result is thus quite consistent with the albedo we obtained above, especially since our darkening hypothesis would indicate that the ramp particle albedo is likely to be somewhat lower than the B ring particle albedo. Clearly, improved knowledge of ring photometry is needed.

The data of EC96 at $1.40r_S$ and $1.60r_S$ can now be presented in several two-color (A_C, $\mathscr{R}$) spaces. For example, the chosen radius in the C ring would appear at one point in an (A_C, $\mathscr{R}_{G,V}$) space and at another point in an (A_C, $\mathscr{R}_{UV,V}$) space. Our results for these two benchmark regions are presented in Fig. 4, and in the slightly different form of A_{UV}, A_V, and A_G in Table I; from these observations, the corresponding values (n_i, a) are directly obtained and tabulated in Table I.

4. POLLUTION TRANSPORT MODEL

In this section we describe the model by which we calculate how "pollution" builds up in the rings due to meteoroid bombardment, how it is redistributed by ballistic transport, and how it is manifested in ring particle properties.

4.1. Radial Profiles of Ring Optical Depth, Mass Density, and Opacity

The ring optical depth and surface mass density as functions of radius are both critical parameters. The optical depth profile is one we obtained from Voyager imaging data (e.g., Dones *et al.* 1993, Cuzzi *et al.* 1984). It has lower resolution (roughly 25 km) than the Voyager PPS and UVIS data, but better signal to noise ratio, especially in low optical depth regions.

The surface mass density is then determined from the *opacity* $\kappa(r) = \tau(r)/\sigma(r)$. The surface mass density of the rings $\sigma(r)$ has only been measured in several isolated spots, usually spiral density wave regions. As the optical depth is known in these regions as well, κ can be determined in these discrete and widely separated sites (see, e.g., tabulations in Cuzzi *et al.* (1984) and Lissauer and Cuzzi (1985)). Only two such locations are found in our region of interest: the Maxwell ringlet and the Janus 2:1 density wave. A profile of higher radial resolution is needed to see if the pollution transport process by itself can account for the detailed *shape* of radial color profiles across the rings.

Given that the ring particle size distribution, in most regions, is well approximated by a power law $N(R)dR = N_0R^{-s}dR$, with lower and upper radius limits (R_1, R_2), it is simple to show that (for the common index $s = 3$)

$$\kappa = \frac{\tau}{\sigma} = \frac{\int_{R_1}^{R_2} \pi R^2 N(R)\, dR}{\int_{R_1}^{R_2} \frac{4}{3}\pi\rho R^3 N(R)\, dR} \approx \frac{3\ln(R_2/R_1)}{4\rho R_2}. \tag{14}$$

For slightly different power law slopes in the range $2 < s < 3$, slightly different normalization constants appear and the dependence on R_1 vanishes. For $s > 3$, dependence on the lower cutoff becomes increasingly important. Here, we assume $s = 3$. Then, with other parameters fixed, and allowing for a weak dependence on R_1, the opacity depends esssentially on the radius of the largest particle R_2.

Showalter and Nicholson (1990) have discovered a technique for determining, essentially, this parameter. Their method makes use of "noise-like" fluctuations in the counts observed in short time samples by the Voyager PPS experiment. They present plots of the parameter $Q(r)$,

$$Q = \pi\left(\frac{R_{\text{eff}}}{45\ \text{m}}\right)^2, \tag{15}$$

where the numerical constant applies at the inner edge of the B ring, and (for $s = 3$)

$$R_{\text{eff}}^2 = \frac{\int_{R_1}^{R_2} (\pi R^2)^2 N(R)\, dR}{\int_{R_1}^{R_2} \pi R^2 N(R)\, dR} = \frac{R_2^2}{\ln(R_2/R_1)}. \tag{16}$$

Whether the R_{eff} values refer to "solid" particles or only transient, opaque clumps is not relevant for our purposes; all that matters is the opacity they represent. Substituting Eqs. (15) and (16) into Eq. (14), and adopting $R_1 = 1$ cm, we find

$$\kappa(r) = \frac{3}{4\rho Q^{1/2}}\sqrt{\frac{\pi\ln(10^4 Q^{1/2})}{4\times 10^7\ \text{cm}^2}}. \tag{17}$$

We obtained a file of radially binned Q values from M. Showalter, and from them derived the $\kappa(r)$ values shown as squares in Fig. 5. The scatter in κ in the outer C ring may be real; point-by-point inspection of these values indicates a preferential association of low κ values with rela-

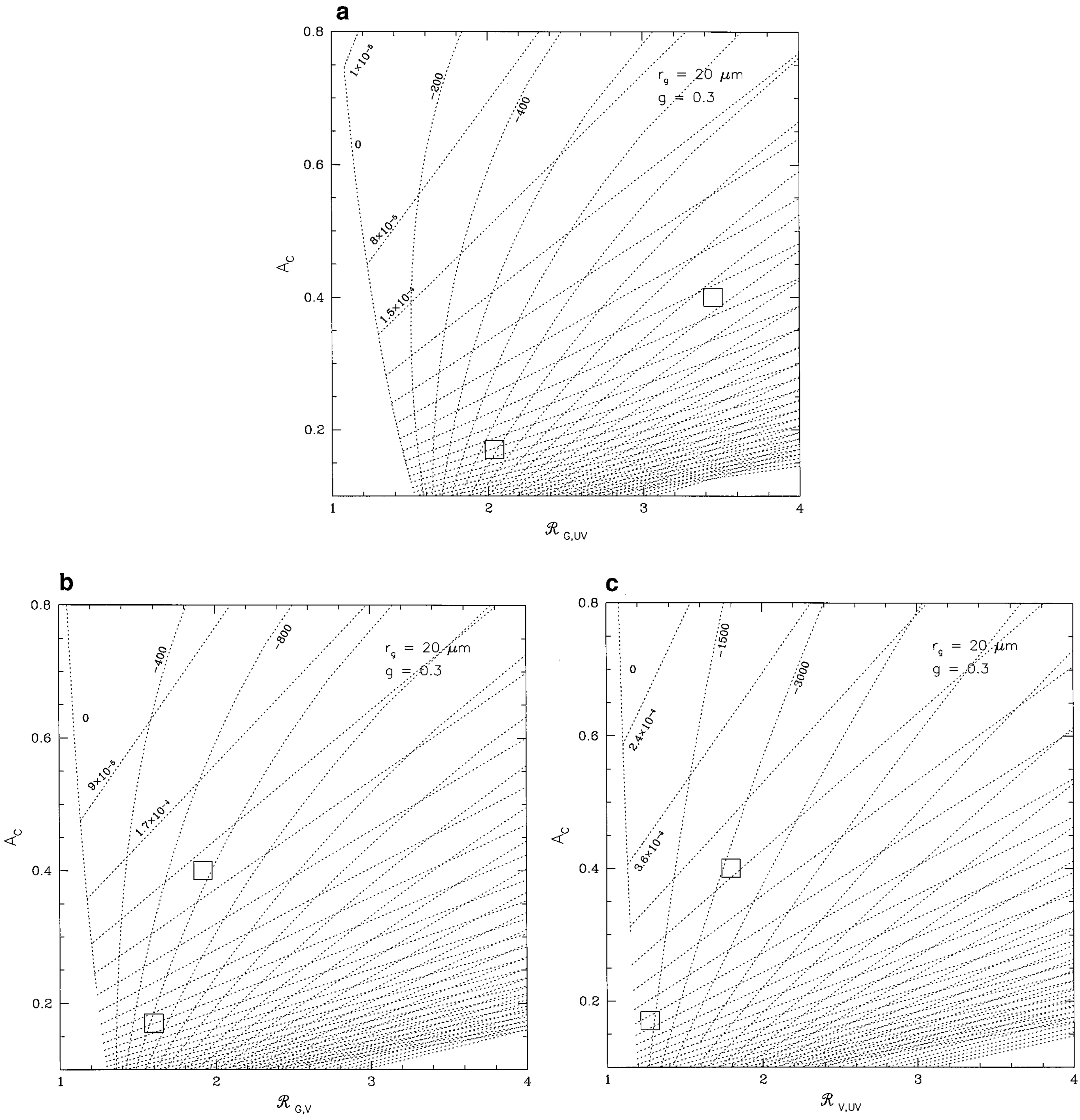

FIG. 4. Three albedo–color phase space plots, analogous to Figs. 2 and 3, but created from Clear filter albedos A_C and color ratios (a) $\mathcal{R}_{G,UV}$, (b) $\mathcal{R}_{G,V}$, and (c) $\mathcal{R}_{V,UV}$. That is to say, while the A_C values are the same here as in Fig. 3, the $\mathcal{R}$ values refer to ratios of reflectivity in different filters and thus differ from those plotted in Fig. 3.

tively higher optical depth "plateaus." This is supported somewhat by comparison of Voyager visual and radio wavelength optical depths obtainable from the PDS rings node. Also shown in Fig. 5 are the opacity values inferred by others from several density waves and ringlets. Due to uncertainties and assumptions built into the simple formulation above, it did not match the observed opacities quantitatively, so we multiplied the simple expression by a con-

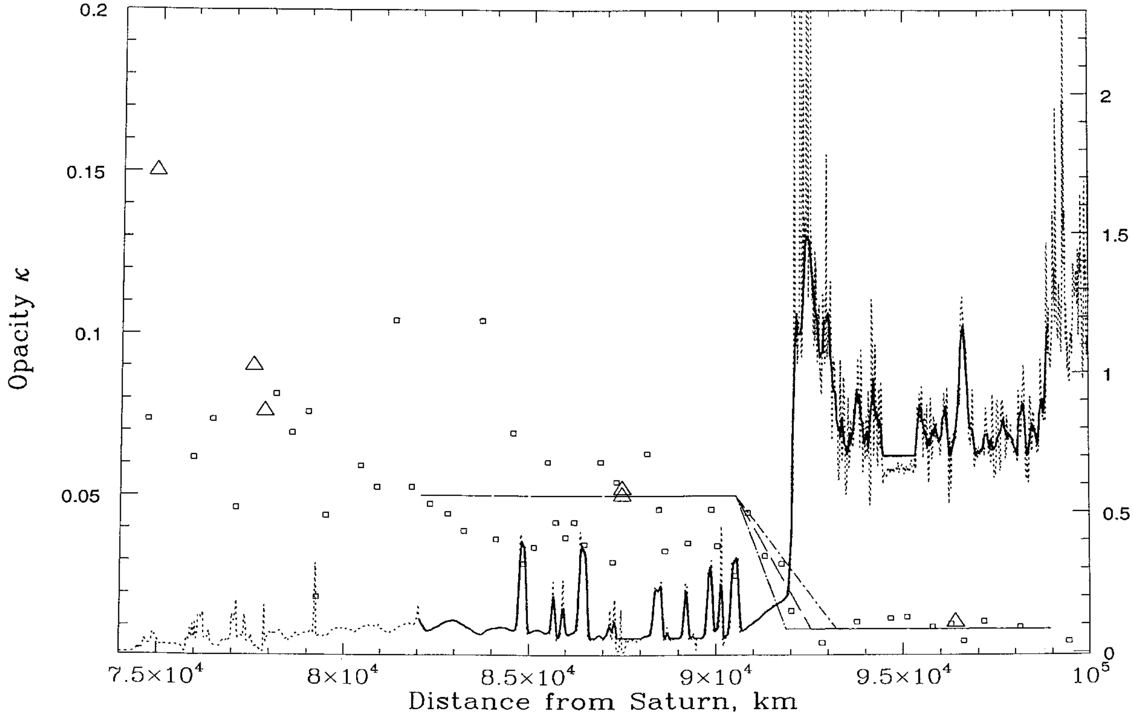

FIG. 5. Estimates of ring opacity κ in the inner B–outer C ring region, from results of Showalter and Nicholson, are shown as squares; these were scaled to match independently known opacity values (shown as triangles; one other known point used is off scale to the right). The baseline radial profile we used for κ is shown as a long dashed line and two "alternate" versions used to explore model sensitivity (Fig. 15) are shown as short dash-dot and long dash-dot lines. The dotted line shows the observed radial profile of optical depth (from Voyager imaging observations), and the heavy solid line shows our model optical depth profile. The inner edge of the B ring is the sharp change in optical depth at 92,000 km.

stant factor of 5.5 in order to bring it into accordance with the actual measurements of κ. For our models, we adopted several straight-line κ profiles, which bound the range of plausible values (see Fig. 5). Essentially, the C ring κ is close to 0.05; the B ring value is more uncertain, due to noise and data gaps in the Q profiles of Showalter and Nicholson (1990). We feel that it is likely that the inner B ring κ lies in the range 0.006–0.012; we adopt the average of these ($\kappa = 0.009$) as the baseline profile (Fig. 5). In Section 5.3.1 we will show the sensitivity of our results to different κ profiles lying within the reasonable range of uncertainty.

4.2. Meteoroid and Ejecta Flux

In this subsection we illustrate the important parameters of the meteoroid bombardment process. In actuality, many of these are determined numerically. The fundamental incident projectile flux (one-sided, flat plate flux, unaffected by gravitational focusing) is $\dot{\sigma}_\infty$. Gravitational focusing by the planet, for an asymptotic relative velocity of 14 km/s, is numerically averaged into a factor F_G at reference radius r_0, for use in calculating the gravitationally focused, two-sided flux $\dot{\sigma}_e(r_0)$ at r_0 in the ring plane, where $r_0 = 1.8r_S$:

$$\dot{\sigma}_e(r_0) = 2\dot{\sigma}_\infty F_G. \tag{18}$$

We obtain the flux crossing the ring plane at other radii using a numerical fit $F(r/r_0)$ to the radial dependence of the calculated focusing (Durisen *et al.* 1992):

$$F(r/r_0) = \left(\frac{r}{1.8r_S}\right)^{-0.8}. \tag{19}$$

Thus the incident flux crossing the ring plane at r is $\dot{\sigma}_e(r) = 2F_G F(r/r_0)\dot{\sigma}_\infty$. The incoming meteoritic material that actually hits the rings (as opposed to merely passing through) is smaller by an *impact probability function* $\mathcal{A}$ which depends on the local optical depth and the various angular aberrations, averaged over the orbit of the ring material (Fig. 15 of CD90). We have parametrized this function as $\mathcal{A} = (1 - e^{-(\tau/\tau_s)^p})^{1/p}$, where the fitting parameters are $\tau_s = 0.515$ and $p = 1.0335$. Then, the local impacting flux is

$$\dot{\sigma}_{im}(r) = \mathcal{A}\dot{\sigma}_e(r_0) = 2\dot{\sigma}_\infty \mathcal{A} F_G F(r/r_0). \tag{20}$$

The mass flux ejected for a given impacting mass flux, say at the reference radius r_0, is

$$\begin{aligned}\dot{\sigma}_{\mathrm{ej}}(r_0) &= 2\dot{\sigma}_\infty(Y_0/10^4)\int_x\int_\Omega y(r_0, x, \Omega)\,dx\,d\Omega \\ &\approx 2\dot{\sigma}_\infty\mathscr{A}(r_0)F_G Y_0.\end{aligned} \tag{21}$$

The full ejecta yield function y defined and derived by CD90 depends on radial distance r and ejecta velocity ($x = v_{\mathrm{ej}}/v_{\mathrm{K}}$) as well as angle Ω (see also Durisen *et al.* 1989, 1992). It incorporates all gravitational focusing and layer impact and escape probabilities. The ejecta yield assumes a v^2 velocity dependence and is normalized to $Y_0 = 10^4$ at 14 km/s impact velocity (Lange and Ahrens 1987). We have numerically validated the final approximation in Eq. 21, and ascribe it to the order–unity cancellation of velocity dependence (>1) and ejecta escape probabilities (<1). Thus, for the purpose of illustration, we can write $\dot{\sigma}_{\mathrm{ej}}(r_0) \approx \mathscr{A}(r_0)\dot{\sigma}_{\mathrm{e}}(r_0)Y_0 = Y_0\dot{\sigma}_{\mathrm{im}}(r_0)$, and for completeness we will ultimately use the fact that the *exact* value of $\dot{\sigma}_{\mathrm{ej}}(r_0)$ is larger by a factor of 1.2 than obtained by using this illustrative value (and the gross erosion time t_{g} thus slightly smaller). The CD90 ejecta distribution y which we use here already allows for all gravitational focusing and this imperfect absorption; therefore the flux $\dot{\sigma}_{\mathrm{im}}(r)$ and its factors $\mathscr{A}F_G F(r/r_0)$ appear only in our direct deposition terms (Eq. (20)).

The *gross erosion time* $t_g(r_0)$ is the time in which a reference ring annulus would disappear due to ejected material *if nothing returned* (Durisen *et al.* 1989, 1992):

$$t_{\mathrm{g}}(r_0) \equiv \frac{\sigma(r_0)}{\dot{\sigma}_{\mathrm{ej}}(r_0)} \approx \frac{\sigma(r_0)}{\mathscr{A}(r_0)\dot{\sigma}_{\mathrm{e}}(r_0)Y_0}. \tag{22}$$

The first equality above is exact and makes use of the full numerically determined normalization in our numerical code, and the subsequent approximation is, as in Eq. (21), for the purpose of illustration. Normalizing time units to t_{g} makes our evolutions independent of the specific value of the projectile mass flux and comparable to evolutions of ring structure (Durisen *et al.* 1992). The age of the rings in real years does depend on the actual numerically determined value of $\int_x\int_\Omega y(r_0, x, \Omega)\,dx\,d\Omega$ to obtain t_{g}. That is, we actually integrate over the realistic ejecta distribution (CD90) at a reference radius and optical depth. In this normalization integral, a factor in $y(r_0, x, \Omega)$ that calculates the return probability of an ejectum is changed to enforce the above definition that *no ejecta returns.*

4.3. Average B and C Ring Compositional Evolution

We first develop an approximate test of the basic hypothesis: that the different "average" color and albedo of the C ring and inner B ring particles, at least, can be explained by exposing initially homogeneous, primarily icy, material to meteoritic infall (this test is implemented in Section 5). The mass fraction f_{e} of extrinsic material at some specific reference point in the B ring as a function of time is

$$f_{\mathrm{eB}} = T\frac{\dot{\sigma}_{\mathrm{B}}\eta}{\sigma_{\mathrm{B}}} = T\frac{\dot{\sigma}_{\mathrm{e}}\eta f_{\mathrm{ext}}\mathscr{A}_{\mathrm{B}}}{\sigma_{\mathrm{B}}}, \tag{23}$$

where T is the exposure time, $\dot{\sigma}_{\mathrm{B}} = \dot{\sigma}_{\mathrm{im}}(\mathrm{B})$ is the amount of incoming mass that actually hits the B ring, f_{ext} is the fraction of this material that is "absorbing" (non-icy), and $\mathscr{A}$ is the impact probability at a reference radius and optical depth. It is assumed that the materials are always and everywhere uniformly mixed. Recalling that $t_{\mathrm{g}} \approx \sigma_{\mathrm{B}}/(Y_0\mathscr{A}_{\mathrm{B}}\dot{\sigma}_{\mathrm{e}})$ (Eq. (22)), one obtains

$$f_{\mathrm{eB}} = \frac{T}{t_{\mathrm{g}}}\frac{\eta'}{Y_0}, \tag{24}$$

where η is the efficiency with which extrinsic material retains its absorptive properties, and we have defined

$$\eta' = \eta f_{\mathrm{ext}}. \tag{25}$$

Our evolutionary times T/t_{g} are thus in units of the gross erosion time. Similarly, for the C ring, taking $\dot{\sigma}_{\mathrm{C}} = \dot{\sigma}_{\mathrm{im}}(\mathrm{C})$, we write

$$f_{\mathrm{eC}} = T\frac{\dot{\sigma}_{\mathrm{C}}\eta}{\sigma_{\mathrm{C}}} = f_{\mathrm{eB}}\frac{\dot{\sigma}_{\mathrm{C}}\sigma_{\mathrm{B}}}{\dot{\sigma}_{\mathrm{B}}\sigma_{\mathrm{C}}}. \tag{26}$$

Equation (26) is rewritten as

$$f_{\mathrm{eC}} = f_{\mathrm{eB}}\frac{\sigma_{\mathrm{B}}\mathscr{A}_{\mathrm{C}}\dot{\sigma}_0 f_{\mathrm{ext}}}{\sigma_{\mathrm{C}}\mathscr{A}_{\mathrm{B}}\dot{\sigma}_0 f_{\mathrm{ext}}} = f_{\mathrm{eB}}\frac{\tau_{\mathrm{B}}\kappa_{\mathrm{C}}\mathscr{A}_{\mathrm{C}}}{\tau_{\mathrm{C}}\kappa_{\mathrm{B}}\mathscr{A}_{\mathrm{B}}} = \frac{T}{t_{\mathrm{g}}}\frac{\eta'}{\zeta Y_0}. \tag{27}$$

where $\kappa = \tau/\sigma$ is the opacity, and we have defined the quantity ζ as

$$\zeta \equiv \frac{\mathscr{A}_{\mathrm{B}}\tau_{\mathrm{C}}\kappa_{\mathrm{B}}}{\mathscr{A}_{\mathrm{C}}\tau_{\mathrm{B}}\kappa_{\mathrm{C}}} \approx \frac{f_{\mathrm{eB}}}{f_{\mathrm{eC}}}. \tag{28}$$

In general, ζ retains the definition above, and has the nominal value $\zeta = 0.0814$, but $f_{\mathrm{eB}}/f_{\mathrm{eC}}$ is not always so easily expressed (Section 4.4.3).

4.4. Basic Transport Equations

Our discussion will follow that of Durisen *et al.* (1989, 1992); some readers might prefer to jump to Section 5 after completing section 4.4.1. The process is illustrated schematically in Fig. 6. For convenience we repeat here the basic equations of mass and angular momentum transport associated with the ballistic transport (BT) process (Durisen *et al.* 1989, Eqs. (3)):

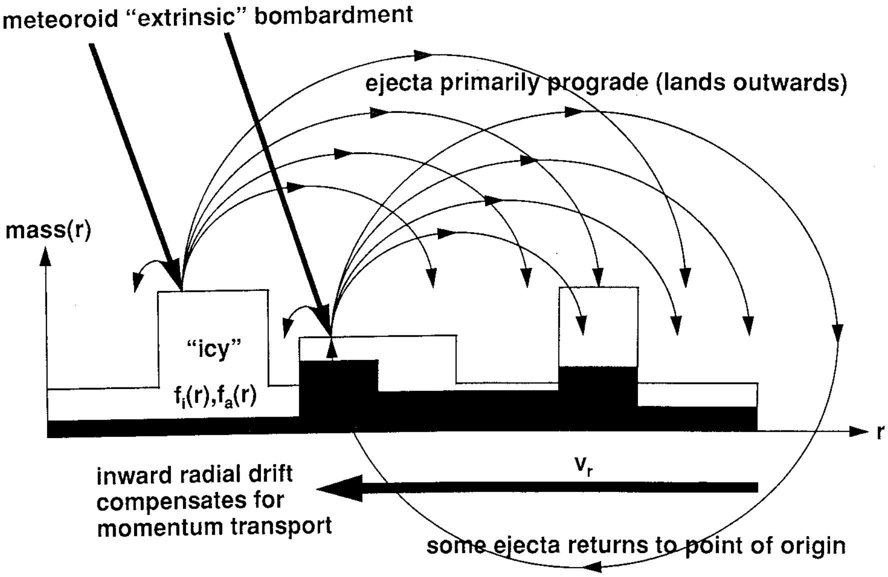
meteoroid "extrinsic" bombardment
ejecta primarily prograde (lands outwards)
mass(r)
"icy"
f_i(r),f_a(r)
r
inward radial drift compensates for momentum transport
v_r
some ejecta returns to point of origin

FIG. 6. Schematic of the pollution transport process, as described in the text (Section 4). The various plateaus represent radial distribution of mass density; shaded regions represent the variable fraction that is non-icy. Outward meteoroid ejecta is indicated, as well as the associated inward radial drift.

$$\frac{\partial \sigma}{\partial t} + \frac{1}{r}\frac{\partial}{\partial r}(\sigma r v_r) = \Gamma_m - \Lambda_m. \tag{29}$$

In the above mass conservation equation (29), the change in surface mass density σ at radius r in the rings is composed of direct and indirect contributions. The direct component is the difference between the net mass gain integral Γ_m *at* radius r *from* all other radii, and the net mass loss integral Λ_m *from* radius r *to* all other radii. The indirect term $(1/r)(\partial/\partial r)(\sigma r v_r)$ represents the change in σ due to the divergence of the total radial mass flux σv_r, where v_r is the radial drift velocity v_r. The radial drift results from transport of angular momentum due both to viscosity ν and the ballistic transport process itself,

$$v_r = (v_r)^{\text{ball}} + (v_r)^{\text{visc}}, \tag{30}$$

where

$$(v_r)^{\text{ball}} = \left(\sigma \frac{dh_c}{dr}\right)^{-1} [\Gamma_h - \Lambda_h - h_c(\Gamma_m - \Lambda_m)] \tag{31}$$

and

$$(v_r)^{\text{visc}} = -\frac{3}{\sigma h_c}\frac{\partial}{\partial r}(h_c \sigma \nu). \tag{32}$$

The quantities Γ_h and Λ_h are the direct angular momentum transport analogs of Γ_m and Λ_m, and h_c is the specific angular momentum for circular orbits:

$$h_c = \sqrt{GM_S r}. \tag{33}$$

We calculate the gain and loss integrals Γ_m and Λ_m using a subroutine of the full BT code of Durisen *et al.* (1989), valid for any radial distribution of optical depth, and any ejecta angular and velocity distribution. The strength of the loss and gain integrals depends on the mass flux $\dot{\sigma}_{ej}$ ejected for a given impacting mass flux (Eq. (21) of Section 4.2), which takes account of all relevant projectile aberrations and ejecta escape probabilities (CD90). Use of this subroutine guarantees that all mass transfer budgets are calculated exactly, including all aspects of cylindrical geometry (see Durisen *et al.* 1989, Sections IIc and IId). We adopt the realistic ejecta angular distribution y of CD90, which results in ejecta that are thrown primarily *outward.* Conservation of angular momentum then induces a radial drift that is primarily *inward.* We also adopt a power law velocity distribution similar to that of Durisen *et al.* (1989, 1992). The ejecta velocities were parametrized by $x \equiv v_{ej}/v_K$, where v_K is the local circular orbit speed in the ring plane, and v_{ej} is the grain ejection velocity. The ejecta velocity distribution $f(x)dx$ is the fraction of ejecta mass having speeds in the interval x to $x + dx$. We used up to 20 x-bins evenly spaced in log x for a power law $f(x)$ of the form $f(x) \propto x^{-13/4}$ for $10^{-4} \leq x < 4 \times 10^{-3}$ (see, e.g., Burns *et al.* 1984). Finally, we verified our code against the more elaborate and precise Durisen code and ran a variety of tests to validate the radial and velocity binning used.

4.4.1. Tracking different materials. At this point, our approach diverges from the structural evolution studies of Durisen *et al.* (1989, 1992). Durisen *et al.* (1992) found that constant optical depth regions, and inner edges, can remain more or less unchanged in overall shape, except for fine-scale structural details, as a result of ballistic transport even over as long as $700t_g$. Thus, to conserve computer time, we do not allow the mass density (or optical depth) profiles to evolve. Instead, our evolution code tracks the mass fraction $f_e(r, t)$ of extrinsic absorber, and assumes that the remainder, $(1 - f_e(r, t))$, is primordial material with primarily icy composition.

The impacting material is assumed to be retained locally with efficiency η, and uniformly mixed throughout the local mass density $\sigma(r)$; it would eventually be of interest to explore alternate assumptions, such as that it departs with the locally generated ejecta. Within the combined parameter η' (Eq. (25)), only a constant fraction $f_{ext} \approx 0.5$ of the impinging mass flux is non-icy, and treated as spectrally absorbing in nature; however, the entire incoming mass flux is used to generate ejecta and thus contributes indirectly to the evolution of the ring composition. The ejecta flux is assumed to have the same makeup as the local region, i.e., to be distributed into fractions $f_e(r, t)$ and $(1 - f_e(r, t))$.

We use the subroutine from the full BT code (prior section) to numerically determine a new set of functions $L_{m,h}(r, r')$ which give the mass and momentum loss *from* r to r', including cylindrical geometry effects. These functions, $L_{m,h}(r, r')$, their radial integrals, $\Lambda_m(r) = \int_{r-4xr}^{r+4xr} L_{m,h}(r, r')\,dr'$, $\Gamma_m(r) = \int_{r-4xr}^{r+4xr} L_{m,h}(r', r)\,dr'$, and the corresponding Λ_h and Γ_h (the latter four defined by Durisen *et al.* (1989)) are calculated only once, since they depend only on the radial optical depth distribution and the ejecta velocity distribution; none of these functions are allowed to change with time. The loss functions $L_{m,h}$ are then used to track the variable mass fraction $f_e(r, t) = \sigma_e(r, t)/\sigma(r)$,

$$\frac{\partial \sigma_e(r,t)}{\partial t} = f_{ext}\dot{\sigma}_{im}(r) - f_e(r,t)\Lambda_m(r) + \int_{r-4xr}^{r+4xr} f_e(r',t)L_m(r',r)\,dr' \tag{34}$$

and

$$\frac{\partial \sigma_i(r,t)}{\partial t} = (1 - f_{ext})\dot{\sigma}_{im}(r) - (1 - f_e(r,t))\Lambda_m(r) + \int_{r-4xr}^{r+4xr} (1 - f_e(r',t))L_m(r',r)\,dr', \tag{35}$$

where the total surface mass density $\sigma(r) = \sigma_i(r, t) + \sigma_e(r, t)$ does not vary with time. Here, $\sigma_i(r, t)$ is meant to consist of both water ice and a trace primordial, non-icy, coloring agent, and $\sigma_e(r, t)$ consists of extrinsic, absorbing, meteoritic material. Then new mass fractions $f_e(r, t) = \sigma_e(r, t)/\sigma(r)$ are calculated at the end of the time step. Various numerical tests were run to ensure that code resolution was adequate in radius and throw distance.

4.4.2. Inward drift. Even while leaving the mass envelope unchanged, we need to recall that the *reason* for this is that net outward-thrown mass is replaced by net inward-drifting mass (Lissauer 1984, Durisen *et al.* 1989, 1992). Prior work did not distinguish between the type of material which is thrown outward and that which drifts back inward (Fig. 6). However, here we must allow for the fact that outward thrown material *may* be different from that upon which it lands or that which replaces it by drifting inward. Therefore, we must further alter the radial distribution $f_e(r, t)$ by accounting for its inward drift during each time step Δt. To do this we calculate the momentum gain and loss integrals Γ_h and Λ_h and the corresponding drift velocity and allow the mass fraction of absorber to adjust as

$$f_e'(r,t) = \frac{f_e(r,t)\sigma + \Delta(f_e\sigma)}{\sigma + \Delta\sigma}, \tag{36}$$

where the divergences Δ of quantities $q = \sigma, f_e\sigma$ are calculated by

$$\Delta q = -\frac{1}{r}\frac{\partial(rqv_r)}{\partial r}\Delta t, \tag{37}$$

where v_r is obtained from Eqs. (30)–(32). Examples of calculations of the evolution of material from one narrow dark annulus into surrounding regions of constant optical depth, with and without radial drift, are shown in Fig. 7. Consequently, the spreading of compositionally distinct material does indeed look somewhat like a diffusion process in this simple case.

4.4.3. Ballistic transport vs diffusion. Inspection of the terms in our evolution calculation reveals that η', n_{ie}, Y_0, and ζ appear only in the combined form $\eta' n_{ie}/Y_0\zeta$ and in one, but not all, terms in the calculation of f_e. Because our observations constrain the quantity $f_e n_{ie}$, the combined quantity $p \equiv \eta' n_{ie}/Y_0\zeta$ becomes an important similarity or *shape parameter* of the problem (Section 5.3.1). This similarity of radial model color profiles with the same shape parameter p is not perfect, because p does not appear in *all* terms involving f_e. Deviation from strict dependence of the shape parameter also arises due to nonlinear dependence of ring brightness on $f_e n_{ie}$ (Maxwell Garnett vs simple linear mixing), variation in the magnitude of the direct deposit and ballistic transport terms as a function of the

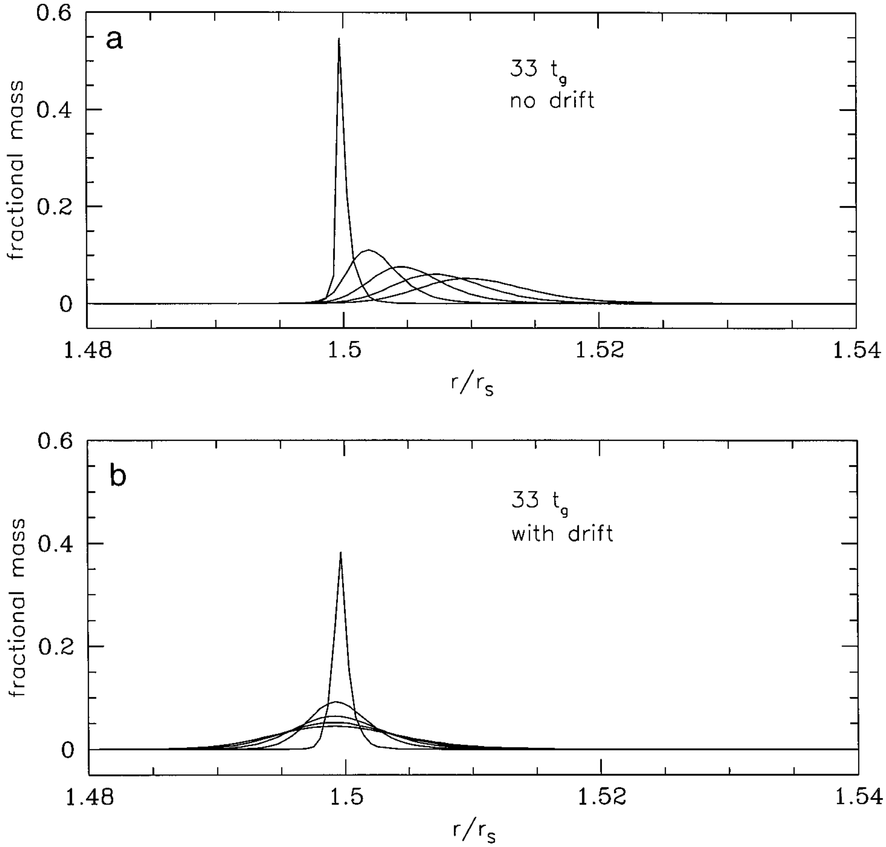

FIG. 7. Examples of the spread of "pollutant" from an initially narrow annulus into surrounding regions with radial drift off (a) and on (b). The profiles of fractional mass of non-icy absorber are uniformly spaced in time from 0 to $33t_g$.

value of $n_{\rm ie}$ itself, and coupling between the C and B ring regions, as described below.

The simple scaling between the C and the B rings represented by Eq. (27) of Section 4.3 assumes that the B and C ring regions in question evolve linearly and independently in time. That is to say, absorbing material at some point was directly deposited there, not carried there by ballistic transport. In fact, because mass is transferred primarily outward with orders of magnitude greater flux than that of the impacting projectiles (due to the large yield factor $Y_0 \sim 10^4$–10^5), the inner B ring begins to receive more pollutant from the C ring as time goes on and the C ring becomes more polluted. In addition, the outer parts of the C ring begin to *lose* polluting material faster than they gain it, due to net ballistic transport outward, once the fractional abundance exceeds Y_0^{-1}. Perhaps most importantly, inward radial drift carries B ring material *into* regions which are nominally part of the C ring. These effects are primarily localized to a region of radial width comparable to the ejecta throw distance δ surrounding the B ring–C ring boundary, and provide its distinctive color profile. However, a rough estimate can be made as to how long the simple scaling remains appropriate before dark C ring material at 1.4 r_S is able to communicate significantly with B ring material at 1.6 r_S.

Although ballistic transport is *not* a traditional diffusion problem, a diffusion approximation can provide useful insights. If ballistic transport *were* a diffusion problem, the time scale for material to be diffused outward from the C to the B ring would be on the order of

$$t_{\rm lim} \sim t_{\rm D} \approx (r_{\rm B} - r_{\rm C})^2/\mathscr{D}, \tag{38}$$

where the diffusion coefficient $\mathscr{D} \sim \delta^2/t_{\rm BT}$, and the time scale $t_{\rm BT} \sim t_{\rm g}(\mathscr{A}_{\rm B}/\mathscr{A}_{\rm C})$. With $(r_{\rm B} - r_{\rm C}) \sim 0.06 r_{\rm S}$, throw distance $\delta = 4 r v_{\rm ej}/v_{\rm K} \sim 10^{-3} r_{\rm S}$ (Durisen *et al.* 1989), and $(\mathscr{A}_{\rm B}/\mathscr{A}_{\rm C}) \sim 3$, the assumption of independence would be valid for 10^3–10^5 $t_{\rm g}$. However, the ejecta are strongly forward-directed, so, in spite of the fact that it takes "two steps out and two steps back" (by drift) one must be a little more careful. Making the more conservative assumption that material is advected rather than diffused,

$$t_{\rm lim} \sim t_{\rm ad} \sim \frac{r_{\rm B} - r_{\rm C}}{\delta}(\mathscr{A}_{\rm B}/\mathscr{A}_{\rm C})t_{\rm g}. \tag{39}$$

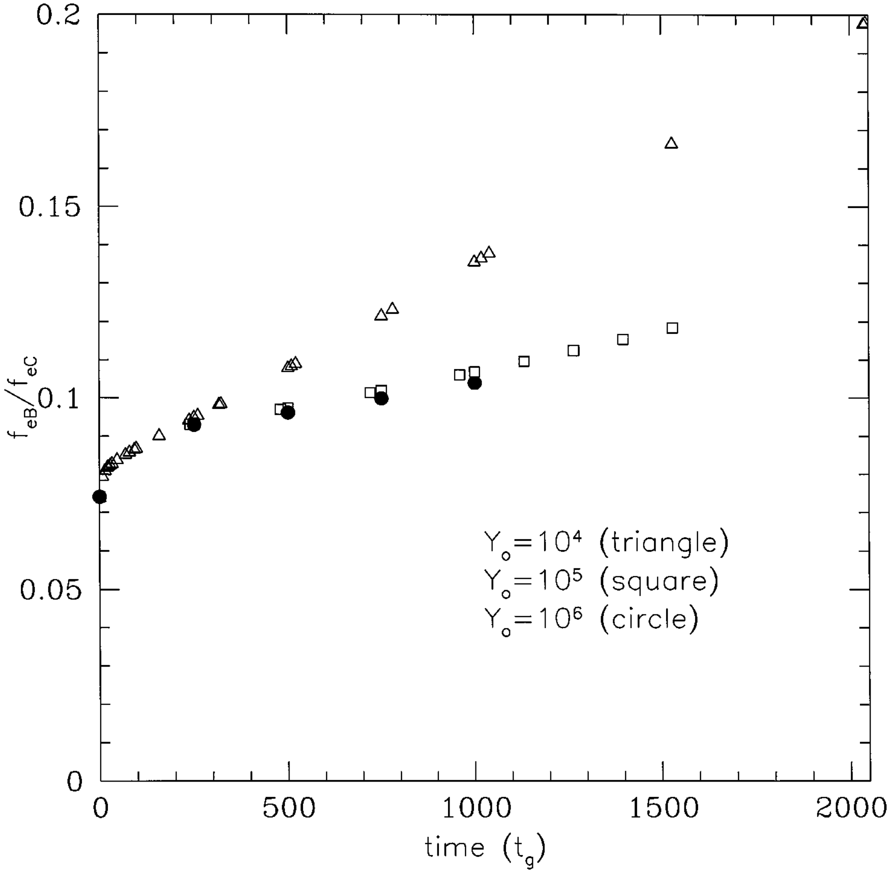

FIG. 8. Evolution trajectories of the ratio of the fractional mass of extrinsic material deposited in the B ring over that deposited in the C ring (f_{eB}/f_{eC}). The ratio follows the same trajectory (but at different rates) for cases that have the same yield factor Y_0 even while they have a range of other model parameters. The limitations of the approximation made in Eqs. (54) (ζ = constant) are easily seen here. The ratio f_{eB}/f_{eC} varies from smaller than, to larger than, our nominal value ($\zeta = 0.0814$), but never by more than a few tens of percent for exposure times we find most plausible ($<300t_g$). Note that there is a qualitative difference in the ratio evolution for the few cases with a yield of $Y_0 = 10^4$. For this small Y_o, the individual trajectories also vary significantly from case to case, even while their ratio is well defined.

This results in a shorter limiting time $\sim 10^2$–$10^3 t_g$. Our numerical studies show a less than 50% deviation of the C ring darkening from the linear relationship (Eq. (27)) by around $500t_g$ (Fig. 8). On time scales longer than these, some of our other simplifying assumptions, such as invariant radial structure, start to weaken. When and if we determine that our simple linear approximation for $f_{eB}/f_{eC} \approx \zeta$ is violated, we obtain f_{eB}/f_{eC} directly from the numerical models, and we always use the numerical result for our final inferences about refractive indices and ring ages.

5. AVERAGE B AND C RING COMPOSITION

We first focus on inferring the average composition of two typical regions straddling the B–C boundary, but sufficiently separated that coupling between them may be neglected (the approach described in Section 4.3). Recall from EC96 (see also Fig. 1) that there are extensive radial ranges more than 30,000 km inward and outward of the exact boundary where the color and albedo are fairly well defined and not strongly variable with radius.

5.1. Inferring Refractive Indices of Different Ring Material

We determine the optical properties of the material which constitutes our two ring reference points, using the color ratio and albedo observations and the phase space model outlined previously in Section 3. For most geological materials, only the imaginary indices $n_i(\lambda) = n_{i,UV} - a(\lambda - \lambda_{UV})$ are of diagnostic importance. We determine the $(n_{i,UV}, a)$ coordinates of the selected B and C ring points directly from their coordinates in $(A_C, \mathcal{R})$ space for a specific choice of grain radius r_g and asymmetry parameter g. We utilize the notation $n_{iB}(\lambda)$ to represent the current imaginary index at $1.6r_S$ in the B ring, and $n_{iC}(\lambda)$ for that at $1.4r_S$ in the C ring.

As mentioned in Section 3, and presented in Fig. 4, each ring radius has coordinates in each of three two-color spaces $(A_C, \mathscr{R}_{G,UV})$, $(A_C, \mathscr{R}_{V,UV})$, and $(A_C, \mathscr{R}_{G,V})$. Any two of these can be used to arrive at a solution for $n_i(UV, V, G)$, but using the third serves as a check on our methods. We determine the n_{iB} and n_{iC} values by direct solution of Eqs. (2)–(8),

$$n_i(\lambda) = \frac{3}{16\pi}\Sigma_\lambda(1-g)\frac{s_\lambda^2}{1-s_\lambda^2}\frac{\lambda}{r_g}, \tag{40}$$

where $\Sigma_\lambda = (1-S_I)/(1-S_E)$. These coefficients are themselves functions of n_r and n_i, but for $n_i \ll 1$, they are dominated by the real refractive index. For uniform mixing, we will show that only a small mass fraction ($\sim 10^{-3}$) of non-icy contaminant material needs to be present; therefore, the effective real refractive index n_r remains very close to that of water ice and Σ_λ is relatively constant, and for the parameters in question, this approach has an accuracy of about 1%. The term s_λ is the Van de Hulst similarity parameter (Eq. (9)):

$$\begin{aligned} s_\lambda \simeq{}& 4.097 + 4.209A_\lambda \\ &- \sqrt{(4.097 + 4.209A_\lambda)^2 - 7.194(1-A_\lambda)}. \end{aligned} \tag{41}$$

In the above equation, A_λ is the Bond albedo at UV, V, or G wavelength, obtained from the observed clear filter albedo and the color ratios through Eqs. (10) and (A2). Values of $n_i(\lambda)$ for any set of A_λ can now be found using Eqs. (40) and (41) (see Table I). Equivalently, appropriate values of $(n_{i\lambda}, a)$ for each wavelength range can be taken from plots of $(A_C, \mathscr{R})$ such as Fig. 4.

At this point, no assumptions have been made about the makeup of the candidate material. *The optical constants extracted from this procedure are those of a uniform local mix of water ice, initial intrinsic non-icy absorber, and extrinsic meteoritic material, and are associated with the present compositional state of the rings in two locations.* Relying on the linear volume mixing approximation, the present-day optical constants $n_{iB}(\lambda)$ and $n_{iC}(\lambda)$ can be formulated as

$$n_{iB}(\lambda) = (1-f_{eB})n_{io}(\lambda) + f_{eB}n_{ie}(\lambda) \tag{42}$$

and

$$n_{iC}(\lambda) = (1-f_{eC})n_{io}(\lambda) + f_{eC}n_{ie}(\lambda). \tag{43}$$

Here, f_{eB} and f_{eC} are the same expressions as (30) and (33) and represent the present fractional mass of extrinsic material in the B and C rings. The "primordial" ring imaginary index n_{io} (recall Section 3.4) is obtained from Eqs. (42) and (43):

$$n_{io}(\lambda) = \frac{n_{iB}(\lambda) - (f_{eB}/f_{eC})n_{iC}(\lambda)}{1-(f_{eB}/f_{eC})} \approx \frac{n_{iB}(\lambda) - \zeta n_{iC}(\lambda)}{1-\zeta}, \tag{44}$$

where we initially approximate f_{eB}/f_{eC} by ζ, defined in Eq. (28), and the other approximations of Section 4.3 also apply. Limitations on this approximation and its use are illustrated in Fig. 8 (Section 4.4.3) and Fig. 10 (Section 5.2.1).

Since water ice is non-absorbing at visual wavelengths, the characteristic "slope" of the primordial mixture retains the spectral behavior of the intermixed absorbing material. That is, $n_{io}(\lambda) \approx f_a n_{ia}(\lambda)$. We then estimate the fractional mass abundance of the initial absorber by adopting imaginary indices $n_{ia}(\lambda)$ for likely candidate materials which have a similar spectral slope. In practice, we calculate effective grain refractive indices $n_{io}(\lambda)$ using Maxwell Garnett mixing theory as variable amounts f_a of the non-icy absorber with imaginary index $n_{ia}(\lambda)$ are added until the inferred values of $n_{io}(\lambda)$ are reached.

The above solution (Eq. (44)) for the imaginary refractive index of the initial state of the rings also automatically determines the product of the mass abundance f_e and imaginary index $n_{ie}(\lambda)$ of the *extrinsic* meteoritic material via Eqs. (42) or (43),

$$\begin{aligned} n_{ie}(\lambda) &= \frac{1}{f_{eB}}[n_{iB}(\lambda) - (1-f_{eB})n_{io}(\lambda)] \\ &= \frac{1}{f_{eC}}[n_{iC}(\lambda) - (1-f_{eC})n_{io}(\lambda)] \end{aligned}$$

or, anticipating that $f_{eB} < f_{eC} < 1$,

$$\begin{aligned} f_{eB}n_{ie}(\lambda) &\approx n_{iB}(\lambda) - n_{io}(\lambda); \\ f_{eC}n_{ie}(\lambda) &\approx n_{iC}(\lambda) - n_{io}(\lambda), \end{aligned} \tag{45}$$

where $f_{eB} \ll 1$ but f_{eC} approaches unity more closely.

5.2. Plausible Intrinsic and Extrinsic Materials

In this section we discuss possible candidates for the initial absorber and extrinsic material, and thereby constrain their relative abundances. Within the pollution hypothesis, no single non-icy material can explain the fact that the darker and more polluted C ring is *less red* than the very red neighboring B ring (Figs. 1, 3, 4). There is more mass in the B ring, so it retains its primordial composition better while the C ring tends to darken and change color more quickly. Suppose the rings began as pure water ice. If the bombarding material is primarily neutral in color, the C ring is easily understood, but the B ring color cannot be produced. Conversely, spectrally red pollutants could color the B ring to its present state, but the C ring would end up considerably *more* red than the B ring, rather than

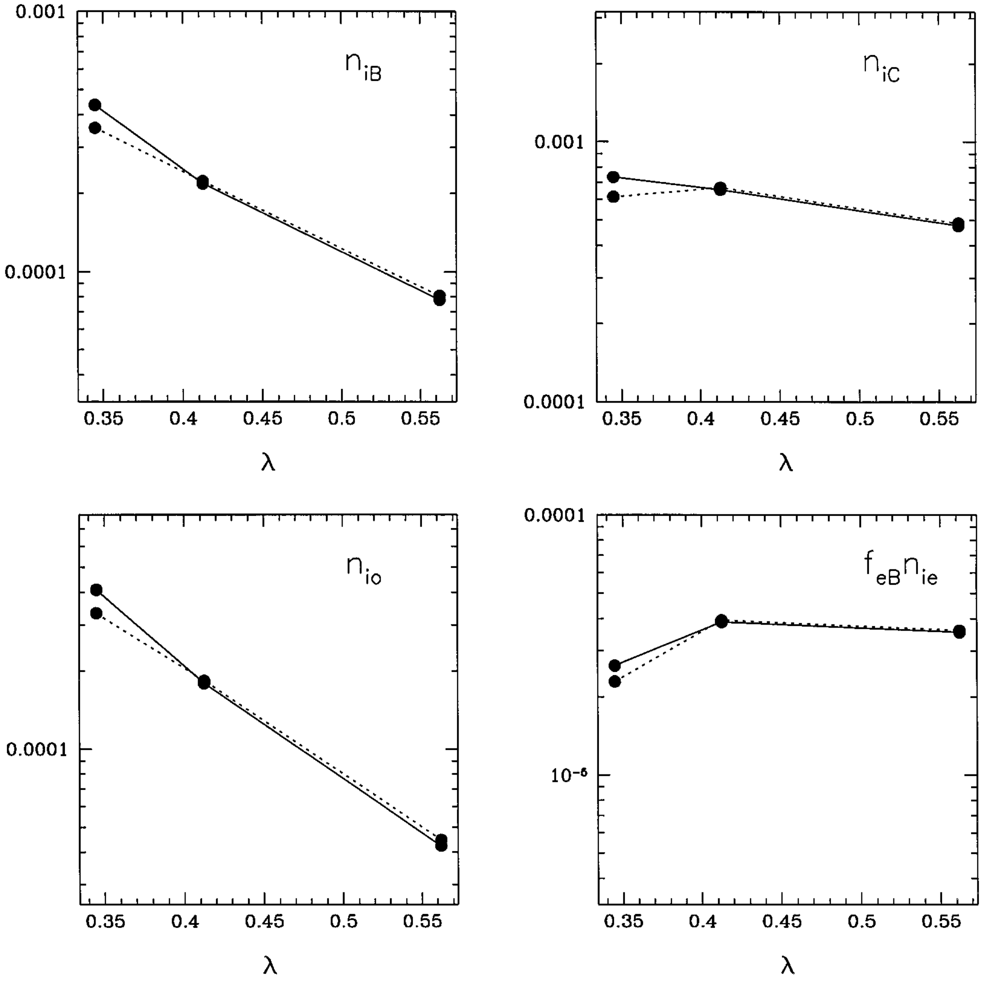

FIG. 9. Plots of our results for the imaginary refractive indices at Voyager *UV*, *V*, and *G* filters. The values at the present epoch (top two plots) are n_{iB} (in the B ring) and n_{iC} (in the C ring) which are determined directly from data presented in, for instance, Fig. 4. We use the methods of Section 5.1 to then infer n_{io} and $f_{\mathrm{eB}}n_{\mathrm{ie}}$ (bottom two plots), which refer to the "primordial," or pre-pollution, and the "extrinsic," or polluting, material respectively. The effects of two different Voyager calibrations are shown (solid lines, atmospheric; dotted, satellite). The present-day B ring value (n_{iB}) is not much changed from the pre-exposure value (n_{io}) because of the B ring's large mass to area ratio. All plots have the same relative range (1.5 orders of magnitude), and all assume $r_g = 20$ μm and $g = 0.3$.

less red as observed. We must therefore consider two separate non-icy materials: one primordial, intrinsic red material which was uniformly distributed in the rings, as well as a highly absorbing, fairly neutral, extrinsic material. We show how the manner of mixing impacts the abundance inferred and consider specific examples of each type of material.

5.2.1. Sensitivity of refractive indices to uncertainties. Using the approach described above and in Section 5.1, we have determined the values of imaginary refractive index currently in the B ring and C ring (n_{iB}, n_{iC}) and then, using Eqs. (44) and (45) of our pollution model, the "primordial" imaginary index n_{io} and the products $f_{\mathrm{eC}}n_{\mathrm{ie}}$ and $f_{\mathrm{eB}}n_{\mathrm{ie}}$. Figure 9 shows values of n_{io} and $f_{\mathrm{eB}}n_{\mathrm{ie}}$ as determined using both Voyager calibrations (see also Section 3.4.1 for more details). The change in the slope of n_{io} due to calibration uncertainty is relatively small and is evident particularly between the *UV* and *V* wavelengths since the primary calibration difference is for the *UV* filter.

The slope of n_{io} is also affected directly by the value of $f_{\mathrm{eB}}/f_{\mathrm{eC}} \approx \zeta$ (Eqs. (28) and (44)); this is illustrated in Fig. 10. A smaller $f_{\mathrm{eB}}/f_{\mathrm{eC}}$ (caused by a larger mass ratio difference between the B and the C rings) would have the effect of slightly increasing the magnitude of n_{io} while any change in the spectral slope is quite small. However, an increase in $f_{\mathrm{eB}}/f_{\mathrm{eC}}$ (related to a smaller mass difference between the B and the C rings) can dramatically change the slope of n_{io}, forcing it to steepen dramatically at the longer wavelengths. In fact, within the perspective of our hypothesis,

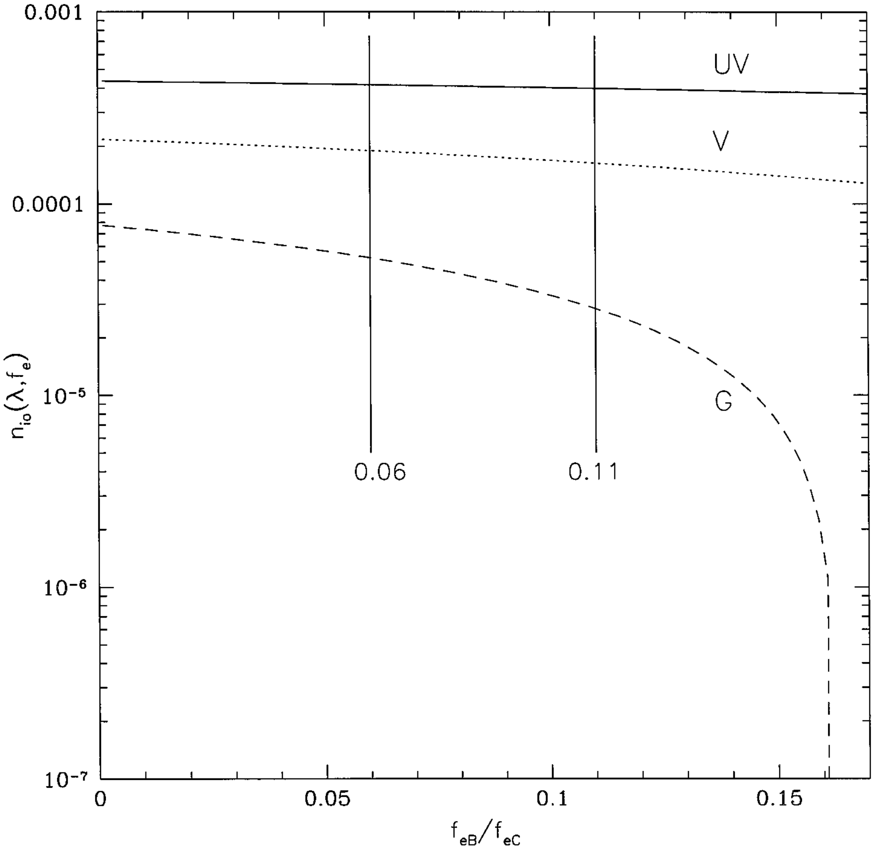

FIG. 10. Plot of $n_{io}(\lambda)$ assuming different values of the ratio f_{eB}/f_{eC}. This ratio varies with ring optical depth and mass density (expressed by the parameter ζ) and, to a slight extent, with the length of exposure (Fig. 8). This figure demonstrates that values of f_{eB}/f_{eC} exceeding 0.16 imply $n_{io}(\lambda)$ values unlike any known material, and values of f_{eB}/f_{eC} exceeding 0.165 or so imply nonphysical values of $n_{io}(G)$. Based on our current knowledge of the rings, plausible values of f_{eB}/f_{eC} lie in the range 0.06 to 0.11, with nominal value 0.082, and thus the form of $n_{io}(\lambda)$ is not especially sensitive to the precise value.

a limit on $f_{eB}/f_{eC} \approx 0.160$ is imposed where $n_{io}(G) \rightarrow 0$. Fortunately, such a large f_{eB}/f_{eC} seems unlikely even given our limited knowledge of the properties of the rings. Current values place the range of ζ, which provides a good approximation to f_{eB}/f_{eC}, between 0.06 and 0.1 (see Section 4.1 for more details). The conclusion is that there is no plausible model parameter that can force the slope of n_{io} to deviate very far from the nominal case. This is a powerful result since the allowable choices for an initial non-icy constituent are then rather well constrained. However, recall that the B and C ring particle albedos each have a significant error bar; this translates to an uncertainty of about 30% in n_{io} and n_{ia}.

Other parameters that can affect the inferred fractional mass abundance of any non-icy constituent are the assumed grain size r_g and the asymmetry parameter g (see Section 3.2). The effects of these parameters on inference of n_i follow directly from Eq. (40); the derived n_i scales linearly with the asymmetry parameter and inversely with grain radius. Since n_i and the fractional amount of impurities appear as a combined factor, the parameters g and r_g influence the amount of non-icy material inferred. A 20-μm typical grain is moderately forward scattering and provides mass estimates consistent with other estimates of the amount of impurities present. Even a choice of $g = 0$ would steepen the values and/or the slope by less than a factor of two, comparable to the effect of the uncertainty in ζ.

5.2.2. Likely intrinsic materials. We relate the average "pre-exposure" refractive index n_{io} to the refractive index and mass fraction of a uniformly distributed candidate non-icy constituent using our Maxwell–Garnett scheme, but express the relationship schematically using the linear mass mixing approximation (assuming $n_i(\text{ice}) = 0$ and $n_{ia} \ll 1$):

$$n_{io}(\lambda) \approx f_a n_{ia}(\lambda). \tag{46}$$

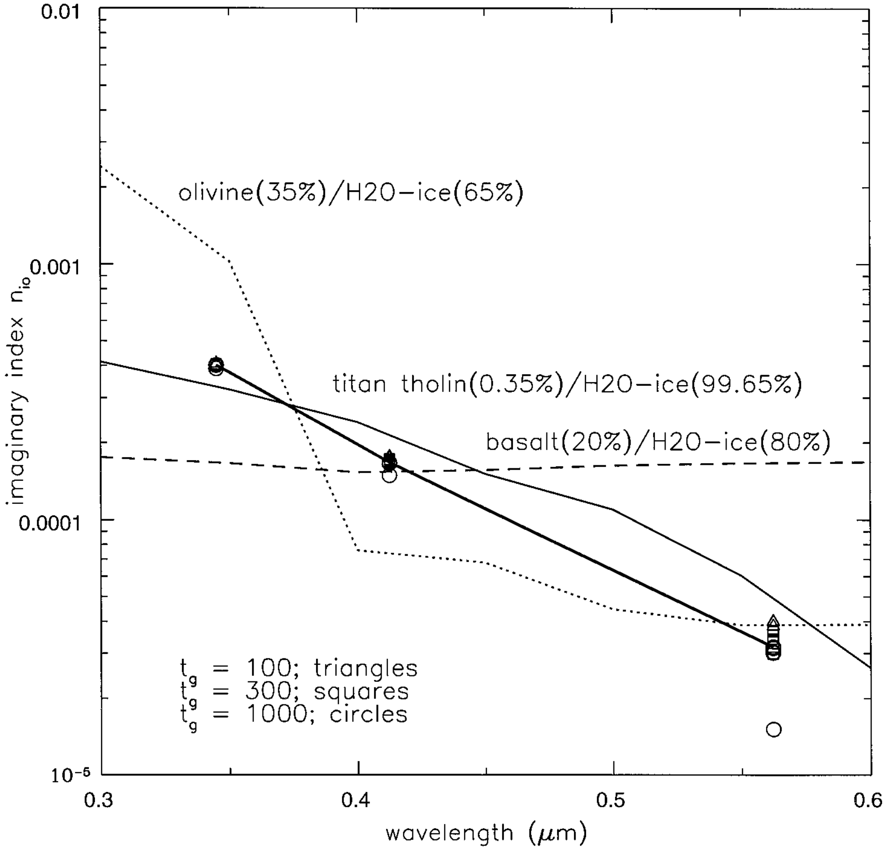

FIG. 11. Plots of our determinations of n_{io} (points, heavy solid line) compared with the quantity $f_a n_{ia}$ for three candidate intrinsic materials: two silicates (olivine, dotted line; basalt, dashed line) and one organic material (Titan tholin, light solid line). The value of f_a is chosen to provide the best overall fit of $f_a n_{ia}$ to n_{io}. Maxwell–Garnett theory was used with refractive indices from Khare *et al.* (1984; Tholin) and Pollack *et al.* (1973; silicates). The modeled points vary slightly with model parameters, but are fairly well constrained (these assume the atmospheric calibration). The Titan tholin provides the best match in spectral shape and mass fraction requires (see Section 5.2.2); in addition to their poor shape fit, silicates also require unacceptably large fractional masses.

A reliable candidate must match the slope between both *G–V* and *V–UV* rather than merely the overall slope between *G–UV*. For each pure candidate material with spectral *shape* matching that observed for the mixture, we use a dilute mixing model such as Eq. (46) to obtain the appropriate mass fraction f_a. We will also employ this approach to the extrinsic non-icy constituent.

Silicates. Silicate materials are cosmogonically prevalent and have been mentioned several times in the past as likely companions to the predominant ice (Section 1). However, primitive anhydrous silicates such as olivine exhibit the wrong spectral shape—too steep between *UV* and *V* and too flat between *V* and *G*—to be compatible with the observed color for either the satellite or the atmospheric calibration case (Fig. 11). In addition, the low n_i for olivine requires a fairly large mass fraction f_a of initial absorber (30%). For basalt, a different silicate, we find that the spectral slope is too small, and as with olivine, a large mass fraction is required (Fig. 11). A hydrated ferric volcanic soil such as palagonite (Clark *et al.* 1990), which has a steep spectral slope, has comparable imaginary indices to the other silicates, and would require a comparably large mass fraction. Varying the Voyager filter calibration has a very small effect compared to the large discrepancies between the observed spectral slope and that produced by these candidate silicates.

Not only are these mass fractions far too large to be compatible with microwave observations, but such large mass fractions would seem to lead inescapably to a prominent silicate spectral feature at approximately 0.9–1.1 μm wavelength–which is absent (we have verified this with our own model calculations). It is possible that the data of Clark (1980) and Karkoschka (1994) imply a *tiny* spectral feature at 1 μm and an even weaker feature at 0.85 μm, possibly indicative of a *much smaller amount* of silicates than can account for the very red slope in visual wavelengths.

Organic solids. A candidate that matches the slope of $n_{io}(\lambda)$ in a satisfactory way is that of the organic solid called Titan tholin (Khare *et al.* 1984). Tholins are organic solids produced by the irradiation of a wide variety of cosmically abundant reducing gases (Sagan and Khare, 1979). The optical constants we utilize for Titan tholin were determined from measurements of dark, red material synthesized by exposure of a simulated Titan atmosphere, to a high-frequency electrical discharge over a 4-month period (Sagan and Khare 1981, 1982, Sagan *et al.* 1984). Estimated errors in the real and imaginary refractive indices are thought to be ±0.05 in n_r and ±30% in n_i (Khare *et al.* 1984, Pollack *et al.* 1994).

In Fig. 11, our determination of $n_{io}(\lambda)$ is compared with refractive indices of a particular mixture of water ice and Titan tholin calculated using the Maxwell Garnett mixing scheme. The spectral slope of Titan tholin provides a fairly good match to our $n_{io}(\lambda)$ values, given the uncertainties. The absolute values of $n_{ia}(\lambda)$ for Titan tholin are so large ($n_{ia} \sim 10^{-1}$) that only small fractional masses of this material are needed to color the rings by the amount required, thus remaining in good agreement with low absorption coefficients inferred from microwave data. By contrast, recall that tens of percent of silicates was needed to accomplish this. We merely take this as evidence that one particular organic material, produced under primitive conditions, is an acceptable candidate. In other work, Wilson *et al.* (1994) and Cruikshank *et al.* (1996) have used Titan tholin refractive indices to obtain a good match to the reflectivity and phase function of the primitive object Pholus. Not all organic materials provide an acceptable fit to $n_{io}(\lambda)$: Carbon-rich organic solids such as poly-HCN (Matthews 1992), types I and II kerogen, and Murchison type II carbonaceous chondrite (Khare *et al.* 1990) do not exhibit a steep enough spectral slope in the visible wavelength range. We discuss these issues further in Section 5.4.

5.2.3. Likely extrinsic materials. We follow the same procedure as for the intrinsic material, seeking plausible extrinsic materials with spectral shapes that fit the wavelength dependence of $f_e n_{ie}$ and use their n_{ie} values to infer the corresponding f_e. The points in Fig. 12 show $f_{eC} n_{ie}(\lambda)$ based upon our solution for $n_{io}(\lambda)$ for the atmospheric and satellite calibration cases. The change in slope of $f_{eC} n_{ie}(\lambda)$ associated with the alternate Voyager calibrations is small (Fig. 9); both calibrations result in a relatively neutral extrinsic pollutant over the visible wavelength range with, perhaps, a weak relative maximum n_{ie} in the *V* wavelength for both cases. Also shown for comparison are values of $n_i(\lambda)$ for various forms of carbon and Halley dust.

Carbonaceous materials. Possible candidates for an extrinsic material with the refractive index we have derived can be found among known astronomical and laboratory primitive materials. It is widely believed that comets are red, but this is not always so, especially in our wavelength range. Chiron, for example, is quite neutral, or even slightly bluish, in color (Fig. 13). Several past workers have measured the reflectance of Halley dust over a considerable wavelength range. At visual wavelengths, the data are not plentiful, but reflectance measurements indicate an overall trend consistent with a neutral color which tends sometimes to reddish (groundbased data from Tholen *et al.* (1986)) and sometimes even to bluish at Voyager wavelengths (spacecraft data such as in Fig. 6 of Krasnopolsky *et al.* (1987)). Inferences of refractive indices from polarization are in good agreement with the shape of our results (Fig. 12; Mukai *et al.* 1986); however, polarization effects are difficult to model for nonspherical particles. Absolute reflectance spectra of powdered samples of natural graphite and synthetic "amorphous carbon" both decrease monotonically from *UV* to *G*, but both exhibit a minimum between 0.4 and 0.5 μm; thus the existence of a relative maximum in n_i at *V*, such as hinted at in our results (Fig. 12), is plausible (Cloutis *et al.* 1994). Spectrophotometry of Comet Schwassmann–Wachmann also show a local minimum in reflectance is observed between 0.4 and 0.5 μm (see Fig. 2 of Cochran *et al.* (1982)). Overall, the imaginary indices of these mostly neutral colored carbonaceous materials are quite large (0.08–0.3) so they are needed in only very small amounts to match our inferred product $f_e n_{ie}$. Exact values are tabulated in Table III, but approximate values $f_{eB} \sim 10^{-3}$ can be obtained simply by dividing plotted values of $f_{eB} n_{ie}$ in Fig. 9 by any typical value of n_{ie} in Fig. 12.

5.2.4. Implications for the origin of the rings. Lebofsky *et al.* (1970) originally pointed out the similarity between the reddish color of the rings and that of Io and even suggested that altered ices might provide a more acceptable fit than silicates. The intrinsic composition of the rings we infer here (water ice and red organic material) implies that the ring material is more similar in genesis to primitive Kuiper and Oort region objects, which formed within the protoplanetary (circum*solar*) nebula, than to the regular satellites, which probably formed in the circum*planetary* nebula (recall Fig. 3). Pluto and Triton are also reddish icy objects that are believed to have formed in heliocentric isolation in the outer Solar System. From the standpoint of the origin of the rings, this would tend to favor the older Roche concept of tidal breakup of a heliocentric passer-by (see Dones 1991) over the impact disruption of a circum-saturnian inner Mimas (see discussions in Harris (1984) and Cuzzi (1995)). Extending this line of speculation a little further, one would expect that the ring parent would need to be large enough to differentiate an icy–organic mantle from residual silicate material. Questions immediately arising, and worthy of further study, include the efficiency of retaining in circumplanetary bound orbits any mantle stripped from a tidally disrupted heliocentric body (which primarily continues on its way; Dones 1991).

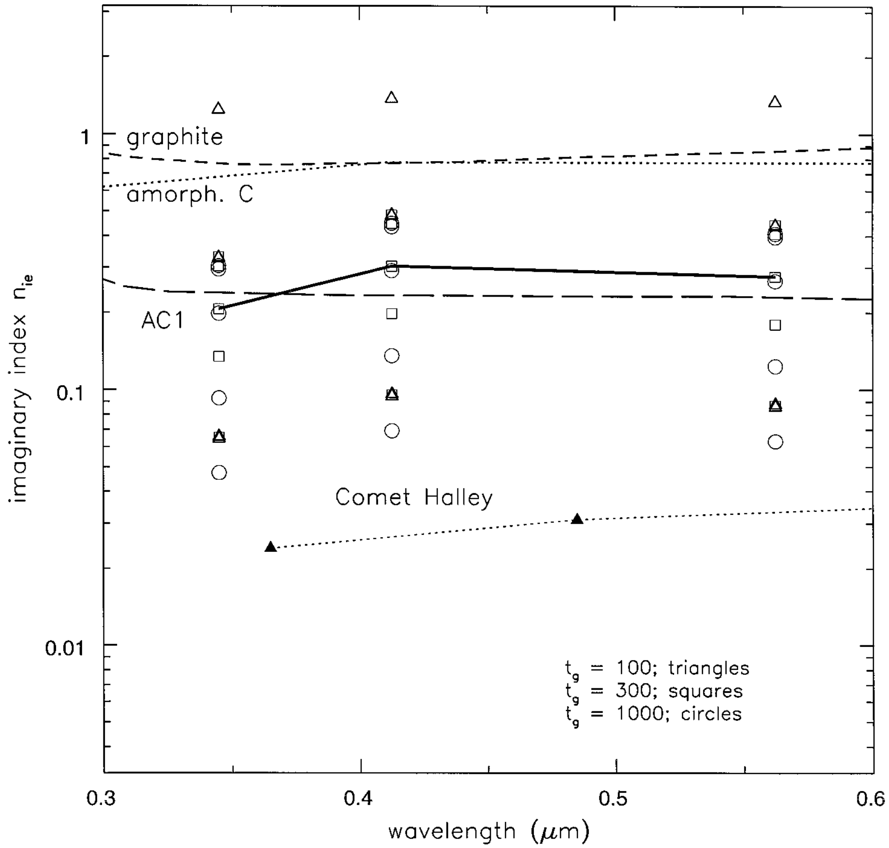

FIG. 12. Plots of our determinations of n_{ie}, assuming the solution for n_{io} shown in Fig. 11, are shown by the points. One set of typical intermediate values for $300t_g$ are connected by a line. Other sets show similar spectral shapes but have magnitudes that vary over a factor of three or so in either direction depending on specific parameters (see Table III). Two sets rely on laboratory soots produced by Bussoletti *et al.* (1987); the set labeled AC1 (Roulean and Martin 1991) represents carbon burned in air and looks similar in shape to values for pure graphite (Asbury Mirco 260 graphite pellet; T. Roush, pers. commun. 1995). These are comparable in magnitude to, but appear to have a slightly different shape, "amorphous carbon" (a reanalysis by Preibisch *et al.* (1993) of the benzene burning or BE data of Bussoletti *et al.* (1987)). Comet Halley dust values are from Mukai *et al.* (1987).

The neutral color of the extrinsic material requires some thought. Even though there are good astronomical prototypes for such material (Halley, Chiron), they are not the norm (see, e.g., Fig. 13); most primitive objects by number have a reddish spectral shape at visual wavelengths. We believe that this puzzle can be explained by allowing for the effects of processing of the small grains that dominate the pollutants. It has long been known that processing of organics by a variety of energy sources (*UV*, charged particles, etc.) causes spectral changes from white to red to black (e.g., Thompson *et al.* 1987). Recently, Cruikshank *et al.* (1996) discuss how energetic processing and the associated decrease of the H/C ratio cause more primitive, hydrogen-rich reddish organics to evolve into more processed, carbon-rich, black ones. The submillimeter grains that dominate ring pollution would be extremely susceptible to evolution of this type, so the small interplanetary projectiles impracting the rings could well be highly evolved, neutral, carbon-dominated material *even if* they originated from the surfaces of more reddish cometary objects. Alternately or additionally, the impact process itself could play a selective role in preserving preferentially the more carbon-rich, hydrogen-poor, material over the more primitive material.

6. RADIAL PROFILES AND RING AGE

Results presented in Section 5.2, using only two representative radii in the C and B rings, demonstrate that the fairly different typical colors and albedos of the C and B ring particles may be simultaneously understood in the context of a meteoroid bombardment model, assuming one initial reddish constituent and one compositionally different (neutrally colored) extrinsic constituent. From our solutions for the combined parameters $f_{eC}n_{ie}$ and $f_{eB}n_{ie}$, we can adopt target values of f_{eC} and f_{eB} based on a plausi-

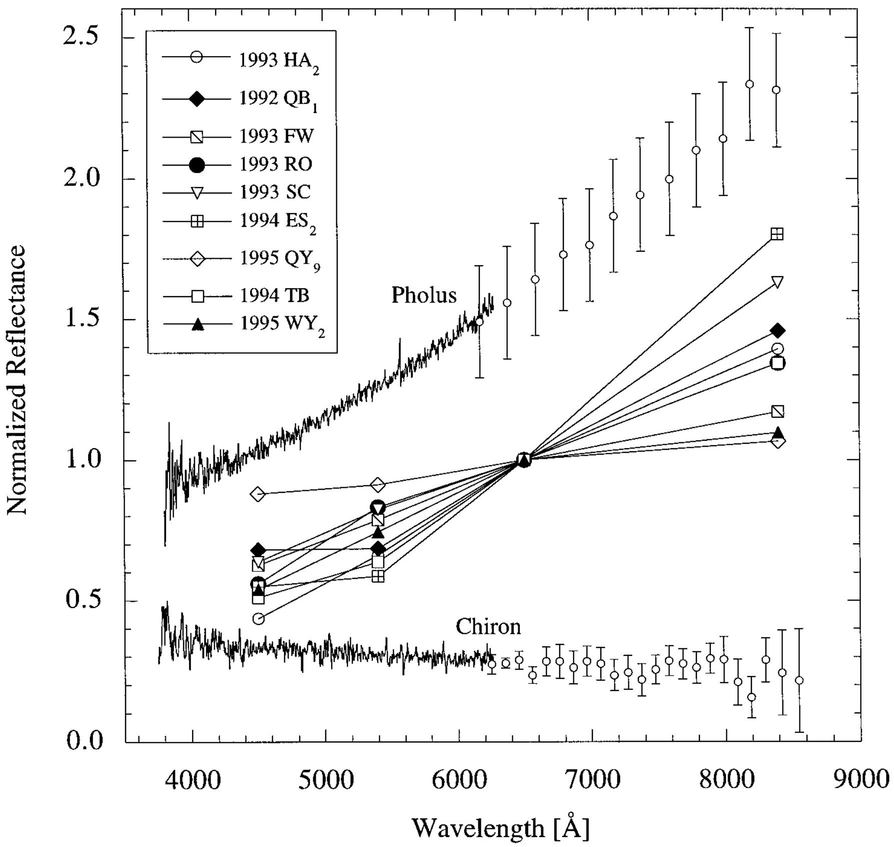

FIG. 13. Normalized spectral reflectance of a variety of outer Solar System objects (from Luu and Jewitt 1996).

ble range of n_{ie} for carbonaceous, highly absorbing material that matches the spectral shape of $f_{\mathrm{eB}}n_{\mathrm{ie}}$ (see, e.g., Fig. 12). The given $f_{\mathrm{e}}n_{\mathrm{ie}}$ implies a certain exposure time in units of t_{g} for any given $\eta' n_{\mathrm{ie}}/\zeta Y_0$ (Eqs. (24), (27)); however, several of these factors are poorly known. Fortunately, we do have other data and a theory which can be used to better constrain these uncertain parameters. The data are the shape of the radial variation of color near the abrupt B–C

TABLE III
Model Parameters

Case	η'	n_{ie}	Y_{o}	t_{g}	$p(\times 10^6)$	$f_{\mathrm{eC}}(\times 10^3)$	$f_{\mathrm{eB}}(\times 10^4)$	Line type
1	0.67	0.0643	10^5	90	5.296	5.020	4.507	Dotted
2	0.134	0.3215	10^5	90	5.296	1.004	0.901	Long dash
3	0.0479	0.09	10^4	91	5.296	3.480	3.004	Short dash
4	0.0134	0.3215	10^4	93	5.296	0.995	0.860	Dot-short dash
5	0.067	0.0643	10^4	96	5.296	5.098	4.416	Solid
6	0.044	0.325	10^5	275	1.757	1.000	0.935	Long dash
7	0.143	0.01	10^4	303	1.757	3.269	3.201	Short dash
8	0.022	0.065	10^4	319	1.757	5.107	5.012	Solid
9	0.11	0.13	10^5	341	1.757	2.459	2.444	Dotted
10	0.15	0.302	10^6	947	0.5569	1.092	1.125	Dot-long dash
11	0.1	0.04532	10^5	957	0.5569	7.096	7.520	Short dash
12	0.05	0.09064	10^5	978	0.5569	3.612	3.843	Dotted
13	0.22	0.198	10^6	1001	0.5574	1.679	1.744	Long dash
14	0.022	0.206	10^5	1530	0.5569	1.618	1.729	Dot-short dash
15	0.0022	0.295	10^4	1001	0.7975	1.168	1.582	Solid

boundary, and the theory is our radial transport model (Section 4.4). Below we describe how this modeling allows us to infer the exposure age in units of the gross erosion time t_g.

6.1. *Radial Shape Modeling*

The final level of detail we present here can be thought of as modeling a diffusion profile with boundary conditions fixed at the values given by our two-point solutions (Section 4.4.3). Even if the values of f_e are fixed at the end points, different model parameters lead to different degrees of internal mixing. For example, if the retention efficiency η' is high, the required pollutant fractions will be reached after only a short exposure accompanied by little radial mixing by ballistic transport; if η' is small, a longer exposure is required to darken the rings, leading to a larger degree of ballistic transport and a more blurred edge profile.

We have run the model for various values of exposure (in units of t_g) within the allowable range. We use the full radial profiles of f_e at each of these exposure times, with their associated solutions for $n_{ie}(\lambda)$ and $n_{io}(\lambda)$ that match the color and albedo properties of our end points at 1.4 and $1.6r_S$, to calculate radial profiles of $\mathscr{R}_{\lambda_1,\lambda_2}$ for comparison with the radial ratio profiles of EC96 (Fig. 1). As expected from the mathematics of the model (Section 4.4.3), we have found that the curves form loose families in the combined parameter $p = (\eta' n_{ie}/\zeta Y_0)$. Figure 14 shows model profiles for various choices of η', n_{ie}, ζ, and Y_0 in plausible ranges that are found to combine in sets with the same p; each family p has a typical characteristic value of $T \approx 100$, 300, and $1000t_g$; profiles for $30t_g$ are, predictably, steeper than those for $100t_g$ and thus not shown. There is some scatter in the precise values of the parameter p within each family, but much less than the order-of-magnitude range of the individual parameters that constitute p (see Table III). To a good approximation, the *shape* of the radial profiles simultaneously constrains the combined parameter $p = \eta' n_{ie}/\zeta Y_0$ *and* the associated exposure age in units of t_g. Extensions of recent work (Brinton and Bada 1996) might eventually place some constraints on η'.

The similarity of the profiles for given (p, t_g) is best in the outer C ring and displays a larger amount of shape variation in the dense inner B ring. However, uncertainties in the opacity κ of this region preclude us placing too much confidence on the details of the profile shape very near to $1.53r_S$; Fig. 15 shows the effect of varying the radial opacity dependence from our nominal set to an only slightly different profile. Overall the most confidence is attached to the general shape in the 1.45–$1.51r_s$ radial range. Furthermore, we ignore color fluctuations associated with the outer C ring plateaus, due to unmodeled opacity fluctuations within these features (Section 4.1). Thus, it seems that the ring exposure is most likely to be in the range of perhaps 200–$500t_g$; certainly the $100t_g$ profile appears too abrupt and the $1000t_g$ profile appears too blurred. Changing the opacity within the dense inner B ring is unlikely to change these conclusions dramatically, and the most likely changes, as shown, would imply *shorter* exposure ages, not longer ones. Our preferred result of $300t_g$ is shorter than the inference of Durisen *et al.* (1992) of 500–$700t_g$ based on "ramp" structural evolution, but given the completely different data, the different models, and the various uncertainties, we regard it as solid support for the hypothesis that meteoroid bombardment and ballistic transport is responsible for both structural and color variations across this key boundary.

In Fig. 16 we compare the model predictions obtained using our two-point n_{io} and n_{ie} values (Figs. 9, 11, 12) with radial ratios of observed color profile (e.g., Fig. 1). The model radial color ratios do an acceptable job of matching the data in all three Voyager ratio profiles. The anomalous color properties of several of the plateaus in the outer C ring are plausibly ascribed to unmodeled opacity variations in these regions (Fig. 5).

6.2. *Inference of Actual Ring Ages*

Converting an exposure age of, say, $300t_g$ to years requires some understanding of the ejecta yield Y_0 and the extrinsic mass flux $\dot{\sigma}_\infty$ (e.g., Eq. (21) of Section 4.2).

6.2.1. Nominal extrinsic mass flux and uncertainty. We first review the status of understanding of mass flux and correct one error in and some minor issues regarding CD90. Pioneer 10 and 11 observations (Humes 1980) measured the cumulative meteoroid number flux from Earth to Saturn. The main conclusions of this work were (a) the distribution of orbital elements of the mass-dominant flux near 5 AU is most consistent with high inclination, high eccentricity material ("Oort cloud" orbital distribution), and (b) the spatial volume density of debris remains nearly constant from 20 to 10 AU. These conclusions refer to particles larger than the threshold for detection of 10^{-9} (Pioneer 10) or 10^{-8} (Pioneer 11) grams (roughly 6 and 13 μm radius, respectively, assuming unit density). The Pioneer 10 and 11 data, for two different threshold masses, have rather similar shapes and thus do not indicate strong variation of the particle size distribution with orbital radius.

Projectile mass flux is the product of projectile mass density and relative velocity; the latter varies with heliocentric distance. The lower projectile *flux* observed by Pioneer at Saturn, relative to that observed at Earth, can be understood simply in terms of all relative velocities being lower by a factor of $\sqrt{10}$ (presuming the same orbital distribution). There is no clear reason for expecting the projectile orbital distribution to change between Earth and Saturn; Fechtig (1984) argues against any significant contribution from the asteroid belt even within the asteroid belt.

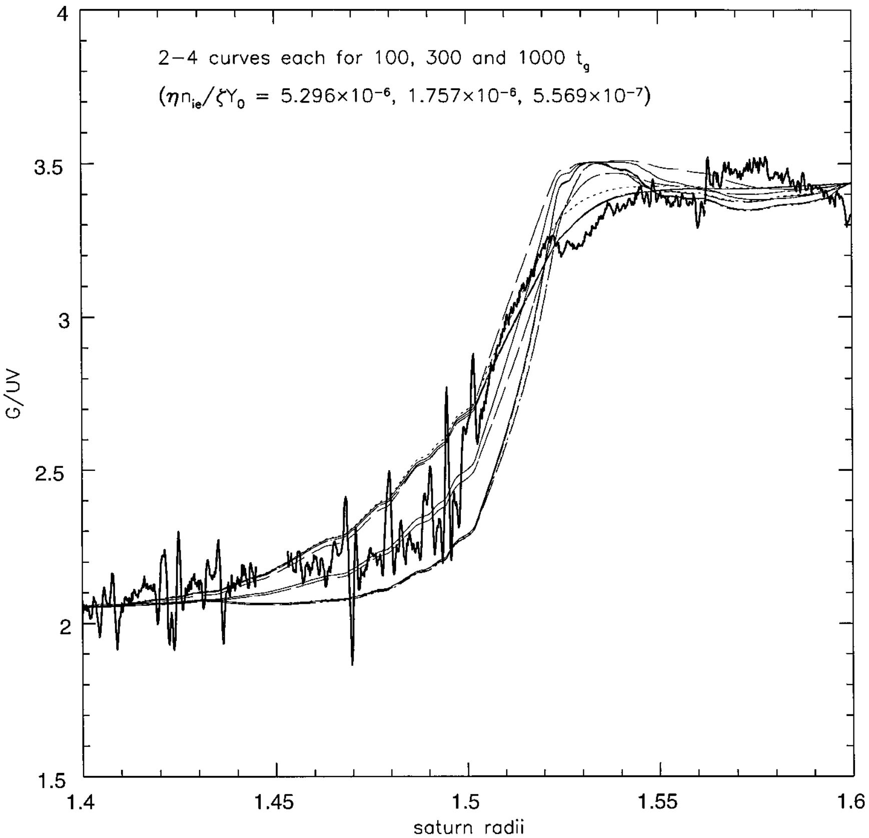

FIG. 14. Figure comparing model families (see Table III for parameter values and line types). The most gradual set is for approximately $1000t_g$ and the most abrupt set is for approximately $100t_g$. The essence of the data (heavy solid line) is best matched by the set for $300t_g$. Distinguishing between curves within a family is less important than realizing the similarity within a family.

Ip (1984) adopted the mass fluxes and particle size distributions of Fechtig *et al.* (1981) at Earth: 7×10^{-17} g cm^{-2} s^{-1}, and scaled it down by a factor between 3 and 18 to that at Saturn based on the radial variation of the flux measured by Pioneer 10 and 11 to obtain $\dot{\sigma}_\infty = 4 \times 10^{-18}$–$2.5 \times 10^{-17}$ g cm^{-2} s^{-1} (allowing for $F_G = 4$). Grün *et al.* (1985) presented a subsequent analysis (at 1 AU) which refined that of Fechtig *et al.* (1981) but did not change the total mass flux significantly. Grün *et al.* (1985) did not publish an integrated mass flux, but instead an integrated mass density of 9.6×10^{-28} g cm^{-3}—consistent with their assumption of a mean relative velocity of 20 km s^{-1} near Earth. The "interplanetary size distribution" of Fechtig (1984) and Grün *et al.* (1985) has a mass peak at a larger size (roughly 100 μm radius) than detectable by Pioneer 10 and 11. Love and Brownlee (1995) used LDEF data to infer a new mass distribution at Earth and obtained a mass flux about 2–3 times larger than that given by Grün *et al.* (1985). The difference is largely due to improved measurements near the 100-μm radius mass peak (S. Love, pers. commun. 1997).

We have reanalyzed our own earlier work (CD90). Our prior value of $\dot{\sigma}_\infty = 4.5 \times 10^{-17}$ g cm^{-2} s^{-1} was obtained as a straight integral over the 1-AU interplanetary flux models of Grün *et al.* (1985, Eq. (A3)) and Ip (1984; Eqs. (1)–(3)). While CD90 recognized and stressed the difference between flux and space density (Section 1), they *incorrectly adopted the Grün et al. (1985) flux at Earth for that at Saturn.* Instead, either the *fluxes* at 1 AU should be decreased according to the Pioneeer data, as done by Ip (1984), or equivalently, a constant *space density* should be combined with a lower *relative velocity*, as done by Moses (1992). We present corrected mass and number flux profiles from CD90, and include Pioneer and Ulysses data, in Fig. 17. To within plausible uncertainties, the Pioneer 10/11 fluxes are in excellent agreement with the Grün *et al.* (1985) fluxes; yet, as discussed above, simple expectations would be that they should be smaller due to the observed falloff with distance (Humes 1980). An explanation might be simply that the Grün *et al.* (1985) fluxes at Earth are too low by a factor of 3 or so (Love and Brownlee 1995). The fluxes at Earth probably contain a significant fraction of "cometary" material (perhaps more than 20% according to D. Brownlee, pers. commun. 1997); this implies that

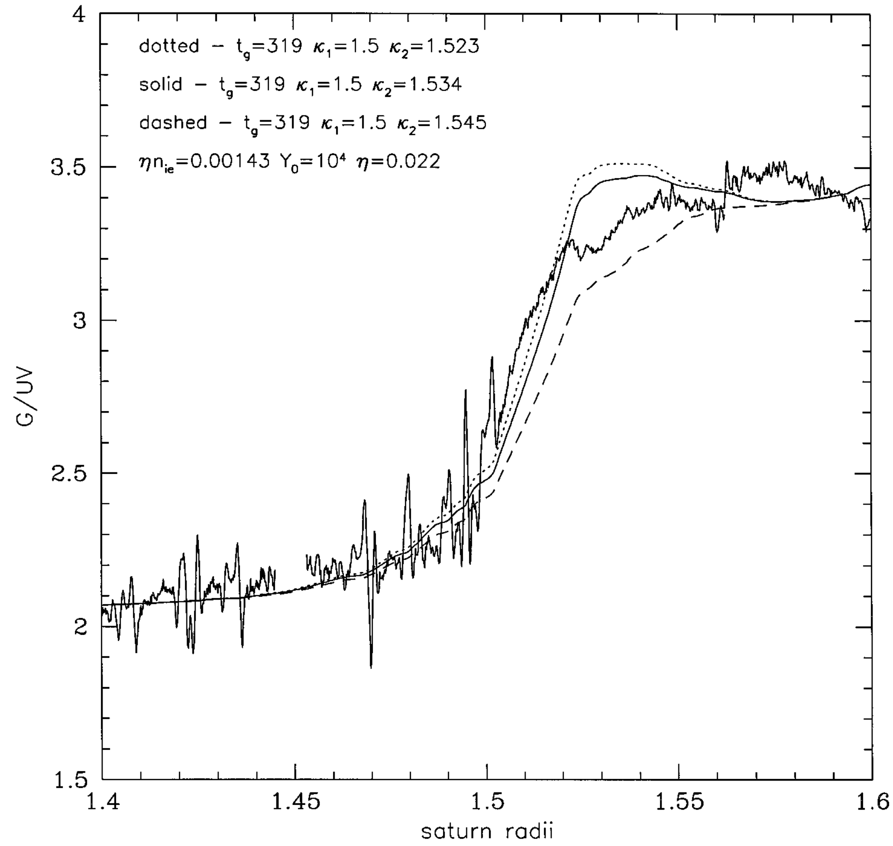

FIG. 15. Model calculations for $300t_g$ for the nominal (dashed curve) and two alternate radial profiles of κ (same legend as in Fig. 5). The short dash-dot profile, which provides a larger κ, or smaller mass-to-area ratio, extending further outward into the B ring, produces a more rounded profile of color ratio—that is, "C ring like" properties extend further into the B ring. The alternate profiles shown here are about as extreme as we feel could be made compatible with the data (see Fig. 5).

the *interplanetary* flux at Earth might be more than 50% "cometary." Thus, the gravitational focusing factor applied by Grün *et al.* (1985) to infer interplanetary values from observed near-Earth fluxes might have been too large, and thus the actual interplanetary flux might be larger yet. These combined factors could explain why the Pioneer 10/11 fluxes seem about as large as the Grün *et al.* (1985) "1-AU" fluxes shown in Fig. 17.

Subsequent work has included a considerable amount of data from Ulysses and Galileo (Grün *et al.* 1993, 1995). These data, also shown in Fig. 17, refer to far smaller particles, with far smaller mass flux than represented by the Pioneer 10/11 population, and in fact are thought to have detected primarily grains of interstellar origin streaming in from the Sun's velocity apex. Preliminary results at larger particle sizes (E. Grün, D. Hamilton, pers. commun. 1996) indicate a flux of material that is lower than, but compatible with, the Humes (1980) number fluxes; the Galileo experiment has only a few detections, so calibration and statistics of small numbers are issues that need to be studied more closely. Overall, because the data are at sizes which are smaller than the plausible peak of the size distribution, the actual mass flux at Saturn has never actually been *observed* and will probably not be *known* until the successful completion of the Cassini mission.

A highly conservative approach might be to adopt a mass flux which assumes the size distribution cuts off at the Pioneer 11 mass threshold (6×10^{-9} g) rather than continuing on to about 10^{-5} g as indicated in the 1-AU size distributions. This would imply $\dot{\sigma}_\infty = 5 \times 10^{-19}$ g cm^{-2} s^{-1}. However, this is no more likely than persistence of the 1-AU size distribution. In fact, Love and Brownlee (1995) note that the knee in the 1-AU distribution might arise only because larger particles cannot reach the Earth by Poynting–Robertson drag within their collisional destruction time, even from the asteroid belt. Consequently, if any change is to be expected in the size distribution going from 1 to 10 AU it might be a *larger* upper size cutoff and thus a larger $\dot{\sigma}_\infty$.

In summary, in spite of a mistaken assertion, the nominal value of $\dot{\sigma}_\infty = 4.5 \times 10^{-17}$ g cm^{-2} s^{-1} adopted by CD90 and in several papers by Durisen and coworkers remains

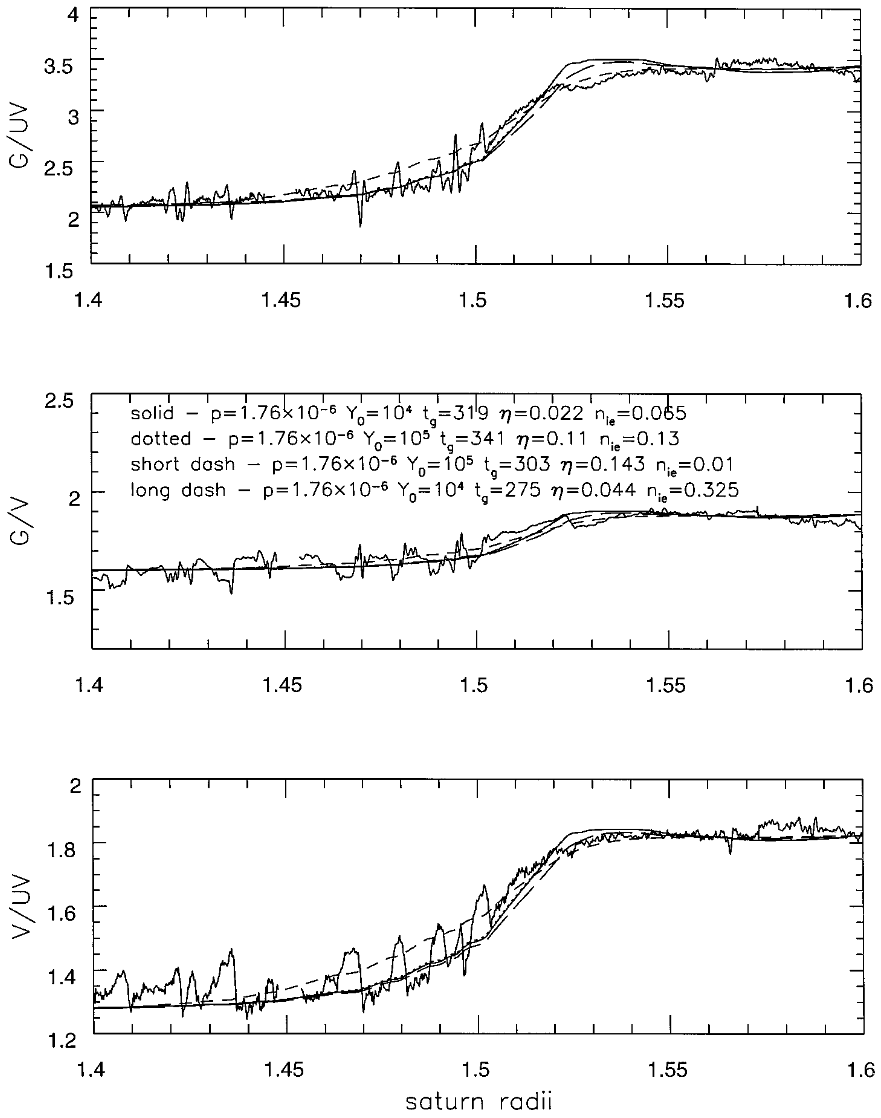

FIG. 16. Radial profiles of Voyager *G*/*UV*, *V*/*UV*, and *G*/*V* ratios, compared with models incorporating the refractive indices of Fig. 9 at $300t_g$. This figure illustrates how all three full radial profiles of color ratio can be simultaneously matched with our final solutions for $n_{io}(\lambda)$ and $n_{ie}(\lambda)$.

plausible; however, it probably has an uncertainty of a factor of 3 or so either way based on the (2σ) error bars in Humes (1980), differences between recent Galileo and Ulysses measurements, differences between Grün *et al.* (1985) and Love and Brownlee (1995), uncertainty in the upper mass cutoff, and various calibration uncertainties (Grün, pers. commun. 1996).

Final details of the flux modeling are discussed in Appendix B.

6.2.2. Nominal ejecta yield and uncertainties. The mass ejecta yield for primarily silicate material bombarding ice has typically been taken to be $Y_0 \approx 10^4$–10^5; substitution into the results of Lange and Ahrens (1987) implies $Y_0 = 3 \times 10^4$ at 14 km/s, which is the value we adopt (see also Croft 1982, Durisen *et al.* 1992, Stern 1986). These values are scaled from experiments at lower impact velocities, and refer to impact into solid icy by macroscopic projectiles. Some lab studies suggest that the yield is smaller for porous targets (Love *et al.* 1993). However, the ring bombardment problem is rather more complex than the lab experiments thus far, unfortunately. The dominant projectile is thought to be in the 10- to 100-μm radius range (Fig. 17); this is not much different in size from a typical regolith grain on a ring particle. Thus, the entire impact-ejecta configuration might not be adequately represented by lab impacts of macroscopic projectiles into smooth, homogeneous, half-spaces. Recent numerical calculations by E. Asphaug (pers. commun. 1996) imply that a somewhat *larger* yield might characterize this situation. Larger yields

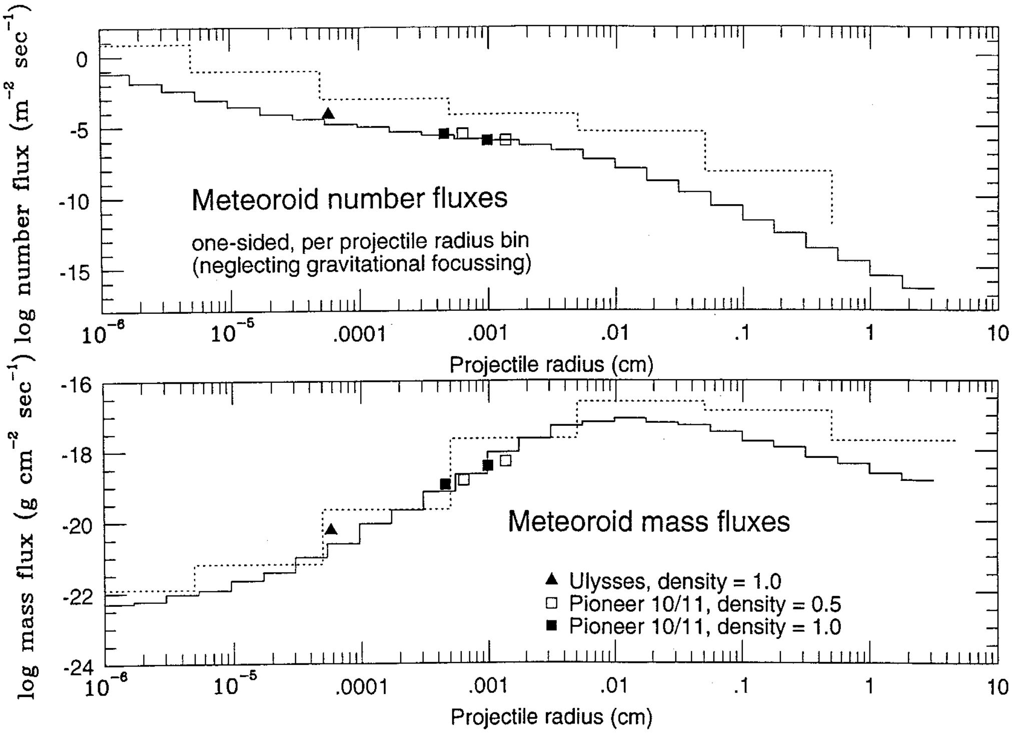

FIG. 17. Meteoroid number and mass flux as a function of particle radius, revised from figure 1 of CD90. Dotted histogram, values presented in CD90; solid histogram, new values corrected for coarse binning and one numerical error. Both profiles are supposedly representative of interplanetary fluxes at 1 AU; Love and Brownlee (1995) find fluxes larger by 2–3 times. Squares: Pioneer 10 and 11 fluxes, for particles larger than thresholds for detection where points are plotted (threshold mass is density dependent; Humes 1980). Triangle: Ulysses fluxes for unit density particles of mass 8×10^{-13} g (Grün *et al.* 1993).

mean smaller t_g, of course. It is also possible that ejecta velocity profiles might differ from those adopted by CD90 from lab impacts into half spaces; these and other avenues for future work have been discussed by Durisen *et al.* (1992). Durisen *et al.* (1992) have also suggested, from their modeling of ring structural evolution, that a somewhat larger effective yield would provide a better fit to the data.

We refer to Eqs. (22) and (18) to calculate t_g,

$$t_g \approx \frac{\sigma(r_0)}{1.2\mathscr{A}\dot{\sigma}_e Y_0} \approx \frac{\sigma(r_0)}{2.4F_G\dot{\sigma}_\infty Y_0}, \tag{47}$$

where the factor 1.2 allows for the exact numerical version of ejecta yield and other parameters are as described in Section 4.4. We adopt $\sigma(r_0) = 100$ g cm^{-2}, $\mathscr{A} \approx 1$ (CD90, Fig. 13), $F_G = 3$, and $\dot{\sigma}_\infty = 4.5 \times 10^{-17}$ g cm^{-2} s^{-1}. Then

$$300t_g \approx 10^8 \text{ years} \left(\frac{3}{F_G}\right)\left(\frac{4.5 \times 10^{-17} \text{ g cm}^{-2}\text{ s}^{-1}}{\dot{\sigma}_\infty}\right)\left(\frac{3 \times 10^4}{Y_0}\right), \tag{48}$$

much less than the age of the Solar System. However, given the uncertainties mentioned above, it might not be possible to *prove* at this time that the $300t_g$ exposure age of the rings *is* shorter than the age of the Solar System.

7. SUMMARY OF CONCLUSIONS AND FUTURE WORK

Conclusions

Meteoroid bombardment explains regional variations of ring composition. The meteoroid "pollution" hypothesis explains in a natural way the observation that the A and B ring particles are redder and brighter than the C ring and Cassini division particles.

Organic material the leading contender for ring "redness." No silicates have the appropriate combination of steep spectral slope and high absorptivity to explain the rings' visual color while remaining compatible with microwave observations. We have shown that one of the several organic "Tholins" does so very easily.

Neutral extrinsic material responsible for post-formation darkening. Material with properties like Carbon black,

TABLE IV

Parameter	Definition
a	Slope of imaginary index with wavelength
$A_{C,G,V,UV}$	Ring particle albedo in Voyager clear, green, violet, and UV filters
A_λ	Spherical albedo of a ring particle at wavelength λ
$\mathscr{A}(\tau)$	Probability of meteoroid impact for given τ
η	Retention efficiency of absorbing properties following impact
η'	$\equiv \eta f_{\mathrm{ext}}$
$f_{(\mathrm{i,a,e})}$	Mass fraction (ice, intrinsic absorber, extrinsic material)
$f_{(\mathrm{eB,eC})}$	Current mass fraction extrinsic material in (B, C) ring
f_{ext}	Mass fraction of extrinsic material with absorbing properties
F_{G}	Gravitational enhancement by planet of meteoroid mass flux
g	Regolith grain scattering asymmetry factor
κ	Opacity $\equiv \tau/\sigma$
n_{i}, n_{r}	Imaginary and real refractive indices
$n_{\mathrm{ia,ie}}$	Imaginary refractive index of (intrinsic absorber, extrinsic material)
$n_{\mathrm{iB,iC}}$	Current imaginary index of material in ring (B, C)
n_{io}	Imaginary index of "primordial" material in rings B and C
p	Similarity parameter for radial shape of runs (Section 4.4.3)
p_{v}	Geometric albedo at groundbased visual wavelengths
$p_{UV,V,G}$	Geometric albedo in Voyager UV, V, or G filter band
ϖ_λ	Single scattering albedo of regolith grain (excluding diffraction)
q	Phase integral
Q	Ring particle size parameter (Showalter and Nicholson 1990)
r_{g}	Regolith grain radius
r_0	Reference radius in ring plane
$\mathscr{R}_{\lambda_1,\lambda_2}$	Ratio of reflectivity at λ_1 to that at λ_2
σ	Surface mass density
$\dot{\sigma}$	Mass flux
$\dot{\sigma}_\infty$	Unfocussed, one sided, interplanetary mass flux
$\dot{\sigma}_{\mathrm{e}}$	Two sided mass flux arriving at the ring plane
$\dot{\sigma}_{\mathrm{im}}$	Two sided mass flux impacting within the rings
$\dot{\sigma}_{\mathrm{ej}}$	Ejecta mass flux
τ	Normal optical depth
t_{g}	Gross erosion time $= \sigma/\dot{\sigma}_{\mathrm{ej}}$
x	Ratio of ejecta velocity to orbital velocity
Y_0	Mass of ejecta per unit mass of projectile (at 14 km/s)
$\mathcal{Y}$	Distribution of ejecta with angle and optical depth (CD90)
ζ	Combination of B and C ring properties (Eq. (28))

as seen in at least some comets and IDP's, is needed to explain how the darker rings are *less red.*

Radial profiles further support ballistic transport mechanism and provide constraint on ring age. The good agreement between the model gross erosion times compatible with the observed radial color profile and inferences reached by Durisen and coworkers based on *structural* properties further supports both hypotheses.

Ring age much less than Solar System age. For the best current estimates of the important parameters (impact yield and meteoroid flux) the ring age is inferred to be on the order of 100 million years.

Future Work

Radially variable viscosity. As discussed in detail by Durisen *et al.* (1992), reasonable viscosity depends not only on ring optical depth but on particle size—especially in the high optical depth limit where nonlocal effects (Wisdom and Tremaine 1988) dominate. A fundamental aspect of our model is radially variable *opacity* κ which implies radially variable particle size (Section 4.1) and thus *viscosity*, but this is not yet incorporated in the model.

Coupled pollution and structural evolution. Our assumption of invariant radial mass density profile is probably not a fundamental flaw in the reasoning, based on structural evolution studies, but it is clearly something that one would like to see handled better. Durisen (pers. commun. 1996) is working on a "fast" version of the structural evolution code which will be combined with our pollution transport modeling in the future.

Groundbased radial profiles of reflectance. Technology has evolved to the point where spatially resolved profiles of the rings should soon be attainable at near-IR wavelengths where diagnostic spectral features of silicates might be found.

Better constraints on impact yield. The situation in which projectiles impact a surface composed of particles of the same size (more or less) needs to be modeled in more detail. Impact yield, ejecta velocity distribution as a function of mass, velocity, and angle, and survival percentage of non-icy material are all parameters that might be better constrained in this way. We will never solidly constrain the ring age from arguments such as those presented here without good knowledge of these parameters.

Better fluxes; better albedos/colors: Cassini! Cassini observations will be essential to provide the projectile flux. We expect the CDA (Cosmic Dust Analyzer) to count particles directly up to 100 μm size or so; another handle on the projectile size distribution might be a better understanding of how the creation of "spokes" relates to impact by particles in the centimeter to meter size range (Goertz and Morfill 1983, Cuzzi and Durisen 1990). Improved color *and albedo* data with good spatial resolution will be needed to extend and improve the analysis presented here. This will require good radiative transfer modeling of the rings as well as new observations.

ACKNOWLEDGMENTS

We thank Paul Bode for providing us with a modified version of a subroutine from the Durisen *et al.* (1989) BT code back in 1990 and Bob

Hogan for helpful suggestions regarding optimization of our overall code. We thank Ted Roush for helpful conversations and for providing us with many refractive indices for silicates of various types. We thank Bonnie Buratti, Marcie Nelson, Paul Helfenstein, Jay Goguen, and Peter Wilson for useful discussions on Hapke albedo modeling, and Dale Cruikshank and Hal Weaver for useful discussions on the colors of material in the outer Solar System. We thank Mark Showalter, Erik Asphaug, Luke Dones, and Jack Lissauer for useful conversations and for performing calculations to help constrain the ring opacity, impact yield, and gravitational focusing factor. We thank Dick Durisen, Luke Dones, and Ted Roush for in-depth manuscript reviews. We thank the Planetary Geology and Geophysics program of the Solar System Exploration Division for its strong support of planetary ring research. We thank the Planetary Rings Discipline Node for providing Voyager radio and stellar occultation data and Robin Canup and John Hillier for useful reviews. During the course of this research, the community has lost two of its brightest stars: Jim Pollack made many contributions to the overall understanding of ring composition and provided numerous discussions about radiative transfer over the years. Carl Sagan was an enthusiastic supporter of this work in particular, and we greatly appreciated his interest and encouragement. Both will be often and fondly remembered in the Cassini era.

APPENDIX A: DETERMINATION OF A_C FROM VALUES AT *UV*, *V*, *G*

In order to calculate the albedo A_C from Bond albedos which we calculate at other Voyager wavelengths using our regolith albedo code, we generate appropriate weighting factors. We begin with our profiles of $(I/F)_\lambda$ as functions of radius. A polynomial fit to the three spectral bands (UV–V–G) is created for each radial bin; the effective wavelengths are obtained using the same weighting functions as in Eq. (A1) below. We average these individual spectra over all radial bins in each main ring to obtain the resulting spectra $\langle I/F\rangle_\lambda$, which are similar to groundbased observations of the spectral reflectivity of the rings as a whole in the visual wavelength range (see, e.g., Fig. 24 of Esposito *et al.* (1984), and Karkoschka (1994)). We then define a scaling coefficient c_C to represent all the unknown (wavelength-independent) scattering functions and to relate $\langle I/F\rangle_\lambda$ for each ring to the corresponding clear filter ring particle Bond albedo A_C,

$$c_C A_C = \frac{\int_\lambda \langle I/F\rangle_\lambda B_\lambda V_\lambda O_\lambda F_C(\lambda)\,d\lambda}{\int_\lambda B_\lambda V_\lambda O_\lambda F_C(\lambda)\,d\lambda} = \overline{I}_C, \tag{A1}$$

where B_λ is the Planck function for the Sun, and O_λ, V_λ, and $F_C(\lambda)$ are the response functions of the camera optics, vidicon, and clear filter, respectively (Danielson *et al.* 1981). The quanity $\overline{I}_C$ is the I/F that would be observed in the clear filter. Then, we note that a "sampled" version of A_C is obtained if the filter function is zero everywhere except for in the *UV* and *G* passbands; specifically, this defines the constants c_{UV} and c_G:

$$\begin{aligned} A_C &\approx \frac{1}{c_C}\left[\frac{\int_\lambda \langle I/F\rangle_\lambda B_\lambda V_\lambda O_\lambda F_{UV}\,d\lambda + \int_\lambda \langle I/F\rangle_\lambda B_\lambda V_\lambda O_\lambda F_G\,d\lambda}{\int_\lambda B_\lambda V_\lambda O_\lambda (F_{UV}+F_G)\,d\lambda}\right] \qquad \text{(A2)} \\ &= \frac{1}{c_C}\left[\frac{c_{UV}\overline{I}_{UV} + c_G\overline{I}_G}{c_{UV}+c_G}\right]. \end{aligned}$$

Then, requiring that $c_{UV} + c_G = 1$,

$$A_C = c_{UV}A_{UV} + c_G A_G. \tag{A3}$$

In Eq. (A3) above, we made use of the fact that, by definition of the normalization constant c_C,

$$c_C A_{UV} = \overline{I}_{UV} = \frac{\int_\lambda \langle I/F\rangle_\lambda B_\lambda V_\lambda O_\lambda F_{UV}\,d\lambda}{\int_\lambda B_\lambda V_\lambda O_\lambda F_{UV}\,d\lambda}, \tag{A4}$$

and similarly for G and V. Note that for the other phase spaces

$$A_C = c_{UV}A_{UV} + c_G\mathcal{R}_{GV}A_V = c_{UV}\mathcal{R}_{UV,V}A_V + c_G A_G. \tag{A5}$$

APPENDIX B: REFINEMENTS TO GRAVITATIONAL FOCUSING

The gravitational focusing expression used by Shoemaker and Wolfe (1982), Lissauer *et al.* (1988), and CD90 ($F_G = 1 + 2GM/Rv_\infty^2$) differs from that used by Morfill *et al.* (1983) and Colwell and Esposito (1992) ($F_G = 1 + GM/Rv_\infty^2$). The difference is between Eq. (5) of Morfill *et al.* (1983) and Eq. (76) of CD90; in the limit of strong gravitational focusing, the difference is a factor of two. We have had several discussions on this subject (J. Colwell, D. Hamilton, L. Dones, J. Lissauer, pers. commun. 1993–1995). The Morfill *et al.* (1983) and Colwell and Esposito (1992) approach envisions the ring and projectiles hitting it as concentric annuli, which is really only appropriate in the case where the projectile velocity is normal to the ring plane. In actuality there is averaging over many relative ring plane orientation angles, and in fact the Shoemaker and Wolfe expression, which scales the flux crossing a disk rather than an annulus, may be an even better estimate once all incident angles are averaged over. There appears to be no simple answer. A good way to determine the gravitational focusing factor is by numerical integration; this is underway (Dones, pers. commun. 1996). In the most probable limit for this case (Oort cloud type orbits), the gravitational focusing is weak and, even using the smaller Morfill/Colwell factor, decreases from our prior value of $F_G = 4.4$. only to $F_G = 2.7$; we will adopt a value $F_G = 3$.

Finally, D. Hamilton (pers. commun.) has called to our attention some inconsistencies in the derivation leading to Eq. A(77ff) of CD90. The correct expression for c_2 is indeed twice that given (i.e., $c_2 = a_S/R_S \sim 25 \times 10^3$; the numerical value cited had an additional error). Because our expression for V_∞^2 lacks the same factor of 2, Eq. (78) of CD90 for R/R_S is actually only a factor of 2 low. The corrections actually provide a better approximation for the value of gravitational focusing factor normally given (which was the main purpose of the section in question).

REFERENCES

Bohren, C. F., and D. R. Huffman 1983. *Absorption and Scattering of Light by Small Particles.* Wiley, New York.

Brinton, K. L. F., and J. L. Bada 1996. A reexamination of amino acids in lunar soils: Implications for the survival of exogenous organic material during impact delivery. *Geochim. Cosmochim. Acta.* **60,** 349–354.

Buratti, B. J. 1984. Voyager disk-resolved photometry of the saturnian satellites. *Icarus* **59,** 392–405.

Buratti, B. J. 1988. Enceladus: Implications of its unusual photometric properties. *Icarus* **75,** 113–126.

Buratti, B. J., and J. Veverka 1984. Voyager photometry of Rhea, Dione, Tethys, Enceladus, and Mimas. *Icarus* **58,** 254–264.

Buratti, B. J., J. A. Mosher, and T. V. Johnson 1990a. Albedo and color maps of the saturnian satellites. *Icarus* **87,** 339–357.

Buratti, B. J., F. Wong, and J. Mosher 1990b. Surface properties and photometry of the uranian satellites. *Icarus* **84,** 203–214.

Burns, J. A., M. R. Showalter, and G. E. Morfill 1984. The ethereal rings of Jupiter and Saturn. In *Planetary Rings* (R. Greenberg and A. Brahic, Eds.), pp. 200–274. Univ. of Arizona Press, Tucson.

Bussoletti, E., L. Colangeli, A. Borghesi, and V. Orofino 1987. Tabulated extinction efficiencies for various types of submicron amorphous carbon grains in the wavelength range 1000 Å–300 μm. *Astron. Astrophys.* Supplement Series **70,** 257–268.

Clark, R. N. 1980. Ganymede, Europa, Callisto, and Saturn's rings: Compositional analysis from reflectance spectroscopy. *Icarus* **44,** 388–409.

Clark, R. N., and T. B. McCord 1980. The rings of Saturn: New infrared reflectance measurements and a 0.326- to 4.08-micron summary. *Icarus* **43,** 161–168.

Clark, R. N., and T. L. Roush 1984. Reflectance spectroscopy: Quantitative analysis techniques for remote sensing applications. *J. Geophys. Res.* **89** (B7), 6329–6340.

Clark, R. N., R. H. Brown, P. D. Owensby, and A. Steele 1984. Saturn's satellites: Near-infrared spectrophotometry (0.65–2.5 μm) of the leading and trailing sides and compositional implications. *Icarus* **58,** 265–281.

Clark, R. N., G. A. Swayze, R. B. Singer, and J. B. Pollack 1990. High-resolution reflectance spectra of Mars in the 2.3μ region: Evidence for the mineral scapolite. *J. Geophys. Res.* **95** (B9), 14463–14480.

Cloutis, E. A., M. J. Gaffey, and T. F. Moslow 1994. Spectral reflectance properties of carbon-bearing materials. *Icarus* **107,** 276–287.

Cochran, A. L., W. D. Cochran, and E. S. Barker 1982. Spectrophotometry of Comet Schwassmann–Wachmann 1. II. Its color and CO emission. *Astrophys. J.* **254,** 816.

Colwell, J. E., and L. W. Esposito 1992. Origins of the rings of Uranus and Neptune. 1. Satistics of satellite disruptions. *J. Geophys. Res.* **97** (E6), 10227–10241.

Cooke, M. E. 1991. *Saturn's Rings: Photometric Studies of the C Ring and Radial Variation in the Keeler Gap.* Unpublished Ph.D. thesis, Cornell University, Ithaca, NY.

Croft, S. K. 1982. Impacts on ice and snow: Implications for crater scaling on icy satellites. *Proc. Lunar Planet. Sci. Conf. 13th,* 135–205.

Cruikshank, D. P., T. L. Roush, M. J. Bartholomew, L. V. Moroz, T. R. Geballe, S. M. White, J. F. Bell III, Y. J. Pendleton, J. K. Davies, T. C. Owen, C. deBergh, D. J. Tholen, M. P. Bernstein, R. H. Brown, K. A. Tryka, and C. M. Dalle Ore 1998. The composition of Centaur 5145 Pholus. *Icarus*, submitted.

Cruikshank, D. P., J. Veverka, and L. A. Lebofsky 1984. Satellites of Saturn: Optical properties. In *Saturn* (T. Gehrels and M. S. Matthews, Eds.), pp. 640–670. Univ. of Arizona Press, Tucson.

Cuzzi, J. N. 1985. Rings of Uranus: Not so thick, not so black. *Icarus* **63,** 312–316.

Cuzzi, J. N. 1995. Evolution of planetary ring–moon systems. *Earth Moon Planets* **67,** 179–208.

Cuzzi, J. N., and R. H. Durisen 1990. Meteoroid bombardment of planetary rings: General formulation and effects of Oort cloud projectiles. *Icarus* **84,** 467–501.

Cuzzi, J. N., P. R. Estrada, and P. Bode 1992. Color, composition, and age at the B–C boundary. *Bull. Am. Astron. Soc.* **24,** 1037.

Cuzzi, J. N., J. J. Lissauer, L. W. Esposito, J. B. Holberg, E. A. Marouf, G. L. Tyler, and A. Boischot 1984. Saturn's rings: Properties and Processes. In *Planetary Rings* (R. Greenberg and A. Brahic, Eds.), pp. 73–199. Univ. of Arizona Press, Tucson.

Cuzzi, J. N., J. B. Pollack, and A. L. Summers 1980. Saturn's rings—Particle composition and size distribution as constrained by observations at microwave wavelengths. II. Radio interferometric observations. *Icarus* **44,** 683–705.

Danielson, G. E., P. N. Kupferman, T. V. Johnson, and L. A. Soderblom 1981. Radiometric performance of the Voyager cameras. *J. Geophys. Res.* **86,** 8683–8689.

Dones, L. 1987. *Dynamic and Photometric Studies of Saturn's Rings.* Ph.D. thesis, Univ. of California, Berkeley.

Dones, L. 1991. A recent cometary origin for Saturn's rings? *Icarus* **92,** 194–203.

Dones, L., J. N. Cuzzi, and M. R. Showalter 1993. Voyager photometry of Saturn's A ring. *Icarus* **105,** 184–215.

Dones, L., M. R. Showalter, and J. N. Cuzzi 1989. Simulations of light scattering in planetary rings. In *Dynamics of Astrophysical Disks* (J. Sellwood, Ed.). Cambridge Univ. Press, U.K.

Doyle, L. R., L. Dones, and J. N. Cuzzi 1989. Radiative transfer modeling of Saturn's outer B ring. *Icarus* **80,** 104–135.

Durisen, R. H., P. W. Bode, S. G. Dyck, J. N. Cuzzi, J. D. Dull, and J. C. White III 1996. Ballistic transport in planetary ring systems due to particle erosion mechanism. III. Torques and mass loading by meteoroid impacts. *Icarus* **124,** 220–236.

Durisen, R. H., P. W. Bode, J. N. Cuzzi, S. E. Cederbloom, and B. W. Murphy 1992. Ballistic transport in planetary ring systems due to particle erosion mechanisms. II. Theoretical models for Saturn's A- and B-ring inner edges. *Icarus* **100,** 364–393.

Durisen, R. H., N. L. Cramer, B. W. Murphy, J. N. Cuzzi, T. L. Mullikin, and S. E. Cederbloom 1989. Ballistic transport in planetary ring systems due to particle erosion mechanism. I. Theory, numerical methods, and illustrative examples. *Icarus* **80,** 136–166.

Epstein, E. E., M. A. Janssen, and J. N. Cuzzi 1984. Saturn's rings—3-mm low-inclination observations and derived properties. *Icarus* **58,** 403–411.

Epstein, E. E., M. A. Janssen, J. N. Cuzzi, W. G. Fogarty, and J. Mottmann 1980. Saturn's rings—3-mm observations and derived properties. *Icarus* **41,** 103–118.

Esposito, L. W., J. N. Cuzzi, J. B. Holberg, E. A. Marouf, G. L. Tyler, and C. C. Porco 1984. Saturn's rings: Structure, dynamics, and particle properties. In *Saturn* (T. Gehrels and M. Matthews, Eds.), pp. 463–545. Univ. of Arizona Press, Tucson.

Estrada, P., and J. N. Cuzzi 1996. Voyager color photometry of Saturn's main rings. *Icarus* **122,** 251–272. Erratum, *Icarus* **125,** 474.

Fechtig, H. 1984. The interplanetary dust environment beyond 1 AU and in the vicinity of the ringed planets (tutorial talk). *Adv. Space Res.* **4,** 5–11.

Fechtig, H., C. Leinert, and E. Grün 1981. Interplanetary dust and zodiacal light. In *Landolt–Börnstein Numerical Data and Functional Relationships in Science and Technology,* Vol. 2, p. 228.

Goertz, C., and G. E. Morfill 1983. A model for the formation of spokes in Saturn's rings. *Icarus* **53,** 219–229.

Gradie, J., P. Thomas, and J. Veverka 1980. The surface composition of Amalthea. *Icarus* **44,** 373–387.

Grossman, A. W. 1990. *Microwave Imaging of Saturn's Deep Atmosphere and Rings.* Unpublished Ph.D. thesis, California Institute of Technology, Pasadena.

Grossman, A. W., D. O. Muhleman, and G. L. Berge 1989. High-resolution microwave images of Saturn. *Science* **245,** 1211–1215.

Grün, E., M. Baguhl, N. Divine, H. Fechtig, D. P. Hamilton, M. S. Hanner, J. Kissel, B.-A. Lindblad, D. Linkert, G. Linkert, I. Mann, J. A. M. McDonnell, G. E. Morfill, C. Polanskey, R. Riemann, G. Schwehm, N. Siddique, P. Staubach, and H. A. Zook 1995. Two years of Ulysses dust data. *Planet. Space Sci.* **43,** 971–999.

Grün, E., H. A. Zook, M. Baguhl, A. Balogh, S. J. Bame, H. Fechtig, R. Forsyth, M. S. Hanner, M. Horanyi, J. Kissel, B.-A. Lindblad, D. Linkert, G. Linkert, I. Mann, J. A. M. McDonnell, G. E. Morfill, J. L. Phillips, C. Polanskey, G. Schwehm, N. Siddique, P. Staubach, J. Svestka, and A. Taylor 1993. Discovery of jovian dust streams and interstellar grains by the Ulysses spacecraft. *Nature* **362,** 428–430.

Grün, E., H. A. Zook, H. Fechtig, and R. H. Giese 1985. Collisional balance of the meteoroid complex. *Icarus* **62,** 244–272.

Hapke, B. 1981. Bidirectional reflectance spectroscopy. 1. Theory. *J. Geophys. Res.* **86,** 3039–3054.

Harris, A. W. 1984. The origin and evolution of planetary rings. In *Planetary Rings* (A. Brahic and R. Greenberg, Eds.), pp. 641–659. Univ. of Arizona Press, Tucson.

Hillier, J., P. Helfenstein, A. Verbiscer, and J. Veverka 1991. Voyager photometry of Triton: Haze and surface photometric properties. *J. Geophys. Res.* **96** Suppl. 19203–19209.

Hillier, J., P. Helfenstein, and J. Veverka 1989. Miranda: Color and albedo variations from Voyager photometry. *Icarus* **82,** 314–335.

Humes, D. H. 1980. Results of Pioneer 10 and 11 meteoroid experiments: Interplanetary and near Saturn. *J. Geophys. Res.* **85,** 5841–5852.

Ip, W.-H. 1984. Ring torque of Saturn from interplanetary meteoroid impact. *Icarus* **60,** 547–552.

Irvine, W. M. 1975. Multiple scattering in planetary atmospheres. *Icarus* **25,** 175–220.

Johnson, T. V., and C. B. Pilcher 1979. Satellite spectrophotometry and surface compositions. In *Planetary Satellites* (J. A. Burns, Ed.), pp. 232–268. Univ. of Arizona Press, Tucson.

Karkoschka, E. 1994. Spectrophotometry of the jovian planets and Titan at 300- to 1000-nm wavelength: The methane spectrum. *Icarus* **111,** 174–192.

Khare, B. N., C. Sagan, E. T. Arakawa, F. Suits, T. A. Callcott, and M. W. Williams 1984. Optical constants of organic tholins produced in a simulated titanian atmosphere: From soft X-ray to microwave frequencies. *Icarus* **60,** 127–137.

Khare, B. N., C. Sagan, W. R. Thompson, E. T. Arakawa, C. Meisse, and P. Tuminello 1996. Kerogen and carbonaceous chondrite organic solids: Optical constants. Submitted for publication.

Khare, B. N., W. R. Thompson, C. Sagan, E. T. Arakawa, C. Meisse, and I. Gilmour 1990. Optical constants of kerogen from 0.15 to 0.40 micron: Comparison with meteoritic organics. In *First International Conference of Laboratory Research for Planetary Atmospheres* (K. Fox *et al.*, Eds.), NASA Conference Publication 3077, pp. 340–356. NASA, Washington, DC.

Krasnopolsky, V. A., V. I. Moroz, A. A. Krysko, A. Y. Tkachuk, G. Moreels, J. Clairemidi, J. P. Parisot, M. Gogoshev, and T. Gogosheva 1987. Properties of dust in Comet P/Halley measured by the Vega-2 three-channel spectrometer. *Astron. Astrophys.* **187,** 707–711.

Lange, M. A., and T. J. Ahrens 1987. Impact experiments in low-temperature ice. *Icarus* **69,** 506–518.

Lebofsky, L. A., T. V. Johnson, and T. B. McCord 1970. Saturn's rings: Spectral reflectivity and compositional implications. *Icarus* **13,** 226–230.

Lebofsky, L. A., and M. B. Fegley, Jr. 1976. Chemical composition of icy satellites and Saturn's rings. *Icarus* **28,** 379–388.

Lissauer, J. J. 1984. Ballistic transport in Saturn's rings: An analytic theory. *Icarus* **57,** 63–71.

Lissauer, J. J., and J. N. Cuzzi 1985. Rings and moons–Clues to understanding the solar nebula. In *Protostars and Planets* (D. Black and M. S. Matthews, Eds.), pp. 920–958. Univ. of Arizona Press, Tucson.

Lissauer, J. J., S. Squyres, and W. Hartmann 1988. Bombardment history of the Saturn system. *J. Geophys. Res.* **93,** 13776–13804.

Love, S. G., and D. E. Brownlee 1995. A direct measurement of the terrestrial mass accretion rate of cosmic dust. *Science* **262,** 550–553.

Love, S. G., F. Hörz, and D. E. Brownlee 1993. Target porosity effects in impact cratering and collisional disruption. *Icarus* **105,** 216–224.

Luu, J., and D. Jewitt 1996. Color diversity among the Centaurs and Kuiper Belt objects. *Astron. J.* **November** 1996.

Lumme, K., and E. Bowell 1981. Radiative transfer in the surfaces of atmosphereless bodies. I. Theory. *Astron. J.* **86,** 1694–1704.

Matthews, C. N. 1992. Dark matter in the Solar System: Hydrogen cyanide polymers. *Origins Life* **21,** 421–434.

McFadden, L. A., J. F. Bell, and T. B. McCord 1980. Visible spectral reflectance measurements (0.3–1.1 μm) of the Galilean satellites at many orbital phase angles. *Icarus* 410–430.

Mischchenko, M. 1994. Asymmetry parameters of the phase function for densely packed scattering grains. *J. Quant. Spectrosc. Radiat. Transfer* **52,** 95–110.

Morfill, G. E., H. Fechtig, E. Grün, and C. Goertz 1983. Some consequences of meteoroid bombardment of Saturn's rings. *Icarus* **55,** 439–447.

Moses, J. I. 1992. Meteoroid ablation in Neptune's atmosphere. *Icarus* **99,** 368–383.

Mukai, T., S. Mukai, and S. Kikuchi 1986. Role of small grains in the visible polarization of comet Halley. In *Proceedings, 20th ESLAB Symposium on the Exploration of Halley's Comet, Heidelberg, October 1986,* ESA SP-250; ESTEC; Noordwijk, Netherlands.

Murphy, R. E. 1973. Temperatures of Saturn's rings. *Astrophys. J.* **181,** L87–L90.

Noland, M., J. Veverka, D. Morrison, D. P. Cruikshank, A. R. Lazarewicz, N. D. Morrison, J. L. Elliot, J. Goguen, and J. A. Burns 1974. Six-color photometry of Iapetus, Titan, Rhea, Dione, and Tethys. *Icarus* **23,** 334–354.

Northrop, T. G., and J. E. P. Connerney 1987. A micrometeorite erosion model and the age of Saturn's rings. *Icarus* **70,** 124–137.

Pollack, J. B., and J. N. Cuzzi 1980. Scattering by non-spherical particles of size comparable to a wavelength—A new semi-empirical theory and its application to tropospheric aerosols. *J. Atmos. Sci.* **37,** 868–881.

Pollack, J. B., D. Hollenbach, S. Beckwith, D. P. Simonelli, T. Roush, and W. Fong 1994. Composition and radiative properties of grains in molecular clouds and accretion disks. *Astrophys. J.* **421,** 615–639.

Pollack, J. B., A. Summers, and B. Baldwin 1973. Estimates of the sizes of the particles in the rings of Saturn and their cosmogonic implications. *Icarus* **20,** 263–278.

Pollack, J. B., O. B. Toon, and B. N. Khare 1973. Optical properties of some terrestrial rocks and glasses. *Icarus* **19,** 372–389.

Porco, C. C., P. D. Nicholson, J. J. Lissauer, J. N. Cuzzi, and L. W. Esposito 1995. Neptune's rings. In *Neptune and Triton* (D. Cruikshank and M. Matthews, Eds.), pp. 703–806. Univ. of Arizona Press, Tucson.

Preibisch, Th., V. Ossenkopf, H. W. Yorke, and Th. Henning 1993. The influence of ice-coated grains on protostellar spectra. *Astron. Astrophys.* **279,** 377–388.

Rages, K., and J. B. Pollack 1980. Titan aerosols: Optical properties and vertical distribution. *Icarus* **41,** 119–130.

Rouleau, F., and P. G. Martin 1991. Shape and clustering effects on the optical properties of amorphous carbon. *Astrophys. J.* **377,** 526–540.

Sagan, C., and B. N. Khare 1979. Tholins: Organic chemistry of interstellar grains and gas. *Nature* **227,** 102–107.

Sagan, C., and B. N. Khare 1981. The organic clouds of Titan. *Bull. Am. Astron. Soc.* **13,** 701.

Sagan, C. and B. N. Khare 1982. The organic clouds of Titan. *Origins Life* **12,** 280.

Sagan, C., B. N. Khare, and W. R. Thompson 1984. Organic matter in the Saturn system. In *Saturn* (T. Gehrels and M. S. Matthews, Eds.), pp. 788–807. Univ. of Arizona Press, Tucson.

Shoemaker, E. M., and R. Wolfe 1982. Cratering time scales for the Galilean satellites. In *Satellites of Jupiter* (D. Morrison, Ed.). Univ. of Arizona Press, Tucson.

Showalter, M. R., and P. D. Nicholson 1990. Saturn's rings through a microscope: Particle size constraints from the Voyager PPS scan. *Icarus* **87,** 285–306.

Smith, B. A., L. Soderblom, J. Beebe, G. Briggs, A. Bunker, S. A. Collins, C. Hansen, T. Johnson, J. Mitchell, R. Terrile, M. Carr, A. Cook, J. Cuzzi, J. Pollack, G. E. Danielson, A. Ingersoll, M. Davies, G. Hunt, H. Masursky, E. Shoemaker, D. Morrison, T. Owen, C. Sagan, J. Veverka, R. Strom, and V. Suomi 1981. Encounter with Saturn: Voyager 1 imaging results. *Science* **212,** 163–191.

Stern, S. A. 1986. The effects of mechanical interaction between the interstellar medium and comets. *Icarus* **68,** 276–283.

Tholen, D., D. P. Cruikshank, H. B. Hammel, J. R. Piscitelli, W. K. Hartmann, and N. Lark 1986. A comparison of the continuum colors of P/Halley, other comets, and asteroids. In *Proceedings, 20th ESLAB Symposium on the Exploration of Halley's Comet, Heidelberg, October 1986,* ESA SP-250, Vol. III, pp. 503–507. ESTEC, Noordwijk.

Thompson, W. R., B. G. J. P. T. Murray, B. N. Khare, and C. Sagan 1987. Coloration and darkening of methane clathrate and other ices by charged particle irradiation: Applications to the outer Solar System. *J. Geophys. Res.* **92,** 14,933–14,947.

van de Hulst, H. C. 1980. *Multiple Light Scattering,* Vols. 1 and 2. Academic Press, New York.

Verbiscer, A., P. Helfenstein, and J. Veverka 1990. Backscattering from frost on icy satellites in the outer Solar System. *Nature* **347,** 162–164.

Warren, S. G. 1984. Optical constants of ice from the ultraviolet to the microwave. *Appl. Opt.* **23,** 1206–1225.

Wilson, P. D., C. Sagan, and W. R. Thompson 1994. The organic surface of 5145 Pholus: Constraints set by scattering theory. *Icarus* **107,** 288–303.

Wisdom, J., and S. Tremaine 1988. Local simulations of planetary rings. *Astron. J.* **95,** 925–940.